JGR Oceans

RESEARCH ARTICLE
10.1029/2018JC014893

# Landslide Material Control on Tsunami Genesis—The Storegga Slide and Tsunami (8,100 Years BP)

**Jihwan Kim**[1,2], **Finn Løvholt**[1], **Dieter Issler**[1], **and Carl Fredrik Forsberg**[1]

[1]Norwegian Geotechnical Institute, Oslo, Norway, [2]Department of Mathematics, University of Oslo, Oslo, Norway

**Key Points:**
- Systematic quantification of the effect of landslide yield strength and remolding on tsunami genesis
- A detailed derivation of a new numerical landslide model is presented
- Landslide parameter ranges are constrained based on Storegga Slide and tsunami observations, which have bearings for future tsunami hazard assessments

**Supporting Information:**
- Supporting Information S1

**Correspondence to:**
F. Løvholt,
finn.lovholt@ngi.no

**Citation:**
Kim, J., Løvholt, F., Issler, D., & Forsberg, C. F. (2019). Landslide material control on tsunami genesis—The Storegga Slide and tsunami (8100 y BP). *Journal of Geophysical Research: Oceans*, *124*. https://doi.org/10.1029/2018JC014893

Received 3 JAN 2019
Accepted 22 APR 2019
Accepted article online 1 MAY 2019



**Abstract** Tsunami generation from subaqueous landslides is controlled by landslide kinematics, which in turn is governed by the material properties of the slide mass. Yet the effect of the material properties on tsunami genesis is poorly understood. Geomorphological observations of landslide runout put constraints on the landslide dynamics. In addition, observations of tsunami runup heights can improve our understanding of how the landslide material transforms from initiation to final runout. The giant prehistoric Storegga Slide off the mid-Norwegian coast caused a well-documented ocean-wide tsunami that offers a unique setting for coupling landslide material models to tsunami generation models. In this study we simulate the dynamics of the Storegga Slide and tsunami using the depth-averaged landslide model BingClaw, which implements visco-plastic rheology and remolding, and couple it to a standard tsunami propagation model. A broad sensitivity study varying the landslide material strength parameters in BingClaw shows that the initial soil yield strength and remolding rate are most important for the tsunami genesis but that the residual strength determined the final runout distance. BingClaw parameters were further optimized to obtain the observed runout distance and to minimize the relative error of the tsunami runup heights. As detailed time-dependent three-dimensional representations of landslide parameters cannot be determined through a field investigation of the landslide itself, these simulations of the Storegga Slide and tsunami can help in the selection of plausible parameter ranges for prognostic modeling in quantitative hazard assessments.

## 1. Introduction

Landslides are the second-most important source of tsunamis worldwide (Harbitz et al., 2014; Løvholt et al., 2015; Tappin, 2010; Yavari-Ramshe & Ataie-Ashtiani, 2016). An important subset, submarine landslides, can exhibit very large volumes ranging up to more than a thousand km$^3$, and they are often tsunamigenic (Løvholt et al., 2017). Despite their large complexity, submarine landslide tsunamis are traditionally treated with simplified source models (Fine et al., 2005; Grilli & Watts, 2005; Hill et al., 2014; Løvholt et al., 2005). The most common example is the block modeling approach, which has been successful in describing certain key historical tsunamis, such as the 1998 Papua New Guinea event (Lynett et al., 2003; Synolakis et al., 2002; Tappin et al., 2008) and the first phase of the 1929 Grand Banks event (Løvholt et al., 2018), both of which were caused by slumps. Such simplified approaches will, however, fall short in describing voluminous submarine landslides where more complex displacement processes such as remolding that alter material behavior and mass during the flow (Elverhøi et al., 2005; Talling, 2014) are important. Consequently, in the absence of relevant modeling approaches, their dynamics has been poorly understood.

It was recently shown that complex landslide dynamics models including remolding are needed to explain both the landslide runout and the tsunami generation for two of the largest landslides in the world, the Holocene landslides Trænadjupet and Storegga offshore Norway (Løvholt et al., 2017). A depth-averaged visco-plastic Herschel-Bulkley type model (BingClaw) appropriate for modeling clay-rich materials was used, and a set of parameters was fitted to reproduce landslide runout and paleo-tsunami observations. However, it was later discovered that simulations with different parameter sets could provide similar descriptions of the historical event. We note that no systematic investigation of the effect of landslide material parameters on tsunami genesis has been conducted to date and that an understanding of how different landslide material properties influence tsunami genesis consequently is lacking. Because tsunami genesis is controlled by the landslide kinematics, presence of tsunami observations will constrain the landslide dynamics better than the landslide runout and morphology alone. Using a simple block as a source, we recently conducted

sensitivity tests for a rock slide tsunami in Iceland that was induced by a volcano flank collapse (Gylfadóttir et al., 2017), linking the landslide kinematics to the tsunami genesis, but without addressing the effect of the landslide material parameters. In contrast, Salmanidou et al. (2017) rigorously constrained the landslide dynamics on the basis of runout data only, that is, in the absence of tsunami observations. To gain deeper insight about how material properties affect tsunami generation, the Storegga Slide allows us to combine all these factors, that is, landslide material models, tsunami models, landslide observations, and tsunami observations.

The primary objective of this paper is a first attempt to quantify more systematically how landslide material parameters are constrained by landslide and tsunami observations. The Storegga Slide offshore the Norwegian coast is used as the test case. The Storegga Slide presents a unique opportunity to obtain stringent bounds on the slide dynamics from back calculations of both the tsunami (through available paleo-tsunami runup heights) and landslide runout (from seabed observations). Moreover, the Storegga Slide is well suited for testing the effect of remolding, as this landslide went through several phases of motion during which the slide material was strongly transformed. The second objective of this paper is to present the first detailed derivation of the numerical debris flow model, *BingClaw*, formulated in terms of Herschel-Bulkley rheology in two horizontal dimensions (2HD). It has a history-dependent yield stress; which means that the yield stress depends on the accumulated bottom shear deformation. BingClaw was briefly presented by Løvholt et al. (2017), but without discussing the physics, mathematical formulation and numerical methods in-depth. While a detailed description of BingClaw is presented in the main body of this paper, additional details of possible limitations of BingClaw given in the supporting information. We also document another model in the supporting information—termed the Kvalstad Retrogressive Block model—in more detail than previously (Kvalstad et al., 2005; Løvholt et al., 2016) and report simulation results using this model.

## 2. The Storegga Slide

The Storegga Slide off the Norwegian west coast took place about 8,100 years ago. With an estimated release volume of 2,400–3,200 $km^3$ (Bryn et al., 2005; Haflidason et al., 2004), it is one of the largest documented landslides in Earth's history (Masson et al., 2006). The preconditioning of the Storegga Slide is believed to be due to interlayering of marine and glacial sediments, which behave differently under loads. The marine sediments generally exhibit strain softening whereas the glacial deposits do not. This layering is conducive to the formation of slip planes in the marine sediments. Furthermore, a persistent high average sedimentation rate, driven mostly by glacial deposition, has allowed high excess pore pressures to develop in the pre-Quaternary oozes. Lateral transfer of the excess pressure to areas with a thinner overburden is believed to have reduced the slope stability in these areas and allowed the development of retrogressive sliding from such a region, perhaps triggered by an earthquake. High-resolution geophysical data combined with geotechnical analysis of the observed landslide morphology also identified the Storegga Slide as a continuous retrogressive event with an extremely long-runout distance of about 400 km for the debris (Bryn et al., 2005; Haflidason et al., 2004; Kvalstad et al., 2005).

The Storegga Slide went through several phases. According to the morphological analysis (Haflidason et al., 2004), the slope first failed retrogressively, starting from near the toe and retreating backward to the upper headwall (Kvalstad et al., 2005). Gauer et al. (2005) strengthened this hypothesis by reproducing the blocky deposits from the last phase of the Storegga slide with Computational Fluid Dynamics (CFD) simulations, in which the slide material is described as a visco-plastic (Bingham) fluid with a history-dependent strain softening of the yield stress and viscosity. The slide deposits at larger water depths reveal a much higher degree of disintegration, hinting that the landslide evolved from a blocky retrogressive slide into a debris flow through progressive breakup and remolding. The Storegga Slide further generated a strong turbidity current with deposits found as far away as the mid-Atlantic Ridge, which indicates large slide velocities.

The Storegga Slide also generated a large tsunami, whose deposits have been identified along the coastlines of the North Sea, Norway (Bondevik et al., 1997, 2005; Romundset & Bondevik, 2011), Scotland and England (Smith et al., 2004), Denmark (Fruergaard et al., 2015), and possibly Greenland (Wagner et al., 2007). With regard to tsunami genesis, the Storegga Slide differs from the majority of smaller tsunami-generating slides, which are of a more impulsive nature, such as the 1998 Papua New Guinea slump (Lynett et al., 2003; Okal & Synolakis, 2004; Synolakis et al., 2002; Tappin et al., 2008) and the slump part of the Grand Banks event Løvholt et al. (2018). It appears to share many features with other voluminous long-runout deepwater events

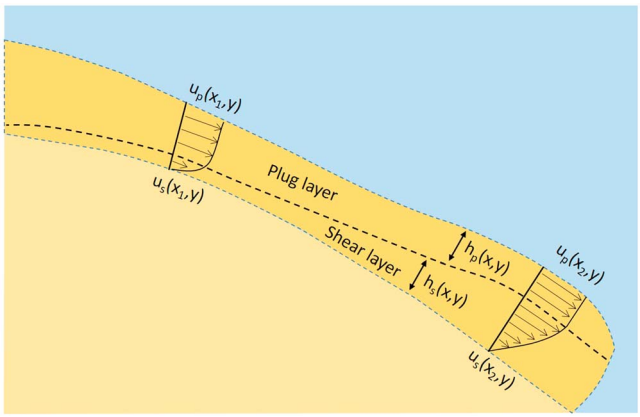


**Figure 1.** Simplified schematic plot of the velocity profile in a depth-averaged Herschel-Bulkley fluid model as employed in this paper. The velocity profile is uniform in the plug layer while it follows a power law with exponent $n + 1$ in the shear layer. As shown in this schematic, the thicknesses and velocities of the plug and shear layers will vary spatially with the $x$ and $y$ coordinates.

such as the neighboring Trænadjupet Slide (Laberg & Vorren, 2000; Løvholt et al., 2017) as well as several large landslides off the U.S. East Coast (Chaytor et al., 2009; Hill et al., 2017; Lee, 2009).

Harbitz (1992), Bondevik et al. (2005), Løvholt et al. (2005), and Hill et al. (2014) assumed rigid-body slides to create the time-varying boundary conditions for simulating the Storegga Slide tsunami. However, this is an overly simplistic representation of the slide, and we will demonstrate in this paper how more realistic landslide models improve the joint description of both the landslide runout and tsunami generation. De Blasio et al. (2005) used the numerical model BING (Imran et al., 2001) for visco-plastic debris flows with Herschel-Bulkley rheology to model the runout in one horizontal dimension (1HD) along a bathymetric transect. To explain the extremely long-runout distance of the Storegga Slide, De Blasio et al. (2005) proposed an extension of BING that included hydroplaning (Mohrig et al., 1998, 1999) and remolding. Because the model of De Blasio et al. (2005) is limited to 1HD, it can describe neither the detailed spatial distribution of the landslide runout nor the tsunami generation in a general bathymetry in two spatial dimensions.

## 3. Numerical Models Used in This Study

### 3.1. BingClaw—A Visco-Plastic Model With Herschel-Bulkley Rheology

#### 3.1.1. Governing Equations

For simple shear, the Herschel-Bulkley rheological model can be described as

$$\left|\frac{\dot{\gamma}}{\dot{\gamma}_r}\right|^n = \begin{cases} 0, & \text{if } |\tau| \le \tau_y, \\ \operatorname{sgn}(\dot{\gamma})\frac{\tau}{\tau_y} - 1, & \text{if } |\tau| > \tau_y, \end{cases} \tag{1}$$

where $\dot{\gamma}$ is the strain rate and $\dot{\gamma}_r$ is the reference strain rate at which the viscous contribution to the shear stress $\tau$ equals the contribution from the yield strength $\tau_y$. $\dot{\gamma}_r$ can be expressed in terms of the dynamic consistency $\mu$ and the flow exponent $n$ as $\dot{\gamma}_r = \left(\tau_y/\mu\right)^{1/n}$. For shear-thinning materials like clay, $0 < n < 1$; $n = 1$ recovers the well-known Bingham rheology as a special case. A Herschel-Bulkley material behaves as a solid where the shear stress is below the yield strength and flows like a power-law fluid above this threshold. A salient feature of a free-surface, gravity-driven flow of a Herschel-Bulkley fluid is the emergence of regions of plug flow where the shear stress falls below $\tau_y$, in particular at the free surface (Figure 1). In the following, we will use the indices $p$, $s$ to indicate quantities that refer to the plug and shear layer, respectively.

We describe the bathymetry by a function $Z = b(X, Y)$ in a Cartesian coordinate system $(X, Y, Z)$, where the $X$ and $Y$ coordinates are horizontal and $Z$ is vertical and the Earth's curvature is neglected. The balance equations governing the flow are, however, formulated in a coordinate system $(x, y, z)$ that is obtained by projecting the $X$-$Y$ plane vertically (i.e., along the $Z$ direction) onto the surface $b(X, Y)$. The $z$ axis is everywhere perpendicular to the local tangent plane $z = 0$ at $b(X, Y)$. This coordinate system is *not* orthogonal. See section S2.1 for a more detailed description and some consequences of its nonorthogonality.

In the momentum balance equations of a depth-averaged model, one needs to express the shear stress at the bed—which depends on the local shear rate at the bed—in terms of the flow depth and the depth-averaged velocity. Doing so requires specific modeling assumptions because depth-averaging eliminates information about the velocity profile. All depth-averaged numerical models with Herschel-Bulkley or Bingham rheology known to us assume that the velocity profile in the shear layer has the form of the steadystate solution. Furthermore, all models except BING (Imran et al., 2001) also postulate that the plug-layer depth, $h_p$, is given by its steadystate value; see, for example, Pastor et al. (2014). This assumption neglects inertial forces, which will increase/decrease $h_p$ if the flow accelerates/decelerates in the direction of gravity. Based on the work of Huang and García (1997), Imran et al. (2001) obtain an approximation to the dynamical plug-layer depth by using separate momentum balance equations for the plug and shear layer, including an exchange term associated with the momentum transferred from one layer to the other when mass moves across the nonmaterial boundary between the two layers. From the layer momenta and the assumed shape of the velocity profile, the layer depths can be calculated algebraically. In 1HD, there are thus three partial differential

equations for the total flow depth and the layer momenta, and one algebraic equation linking the four field variables $h_p$, $h_s$, $h_p u_p$, and $h_s u_s$, where $u_p$ and $u_s$ are the plug and shear-layer velocity, respectively.

BingClaw extends this approach to 2HD, solving the mass balance integrated over the entire flow depth (variable $h = h_p + h_s$) and two separate (vector) momentum balance equations integrated over the plug and shear layer for the variables $h_p$, $h_s$, $h_p \mathbf{u}_p$, and $h_s \mathbf{u}_s$:

$$\partial_t(h_p + h_s) + \nabla \cdot (h_p \mathbf{u}_p + h_s \mathbf{u}_s) = 0, \tag{2}$$

$$\begin{aligned} \partial_t(h_p \mathbf{u}_p) + \nabla \cdot (h_p \mathbf{u}_p \mathbf{u}_p) + g' h_p \nabla(h_p + h_s + b) \\ + \mathbf{u}_p \left[\partial_t h_s + \nabla \cdot (h_s \mathbf{u}_s)\right] = -\frac{\mathbf{u}_p}{||\mathbf{u}_p||} \frac{\tau_y + \tau_d}{\rho_d}, \end{aligned} \tag{3}$$

$$\begin{aligned} \partial_t(h_s \mathbf{u}_s) + \nabla \cdot (\alpha h_s \mathbf{u}_s \mathbf{u}_s) + g' h_s \nabla(h_p + h_s + b) \\ - \mathbf{u}_p \left[\partial_t h_s + \nabla \cdot (h_s \mathbf{u}_s)\right] = -\frac{\mathbf{u}_p}{||\mathbf{u}_p||} \frac{\tau_y f_s}{\rho_d}. \end{aligned} \tag{4}$$

Note that all vectors and the nabla operator are two-dimensional, that is, restricted to the local tangent plane of the bathymetry, which is described by the function $b(x, y)$. The reduced gravitational acceleration (taking into account buoyancy effects) is defined as $g' = g(1 - \rho_w/\rho_d)$, where $\rho_w$ and $\rho_s$ are the water and debris density, respectively. The term $g' h_{p,s} \nabla(h + b)$ combines the slope-parallel component of gravity and the earth pressure gradient; it is discussed more fully in section S2.3.

The coefficient $\alpha$ is the velocity form factor in the shear layer: $\int_0^{h_s} \mathbf{u}^2(z)\mathrm{d}z \equiv \alpha h_s \mathbf{u}_s^2$. $\beta \equiv \dot{\gamma}_b h_s / u_p$ is needed to express the bed shear stress in terms of the flow variables. Assuming the steady-state velocity profile, these coefficients can readily be calculated for the Herschel-Bulkley rheology (Huang & García, 1997; Imran et al., 2001):

$$\alpha = \alpha_2 / \alpha_1^2, \tag{5}$$

$$\alpha_1 \equiv \frac{1}{h_s u_p} \int_0^{h_s} u(z)\mathrm{d}z = \frac{n+1}{2n+1}, \tag{6}$$

$$\alpha_2 \equiv \frac{1}{h_s u_p^2} \int_0^{h_s} u^2(z)\mathrm{d}z = 1 - \frac{2n}{2n+1} + \frac{n}{3n+2}, \tag{7}$$

$$\beta = \left(1 + \frac{1}{n}\right)^n. \tag{8}$$

The right-hand side of the plug-layer momentum balance (3) is given by the shear stress at the interface to the shear layer, which must be $\tau_y$, and the hydrodynamic drag at the free surface, $\tau_d$ (see section 3.1.3). The shear layer is subjected to the shear stresses $+\tau_y$ at the interface to the plug layer and $-\tau_y[1 + (\dot{\gamma}/\dot{\gamma}_r)^n]$ at the bed, equation (4). The net shear stress is thus just the viscous contribution at the bed, given by $\tau_y f_s$, with

$$f_s = \beta \cdot \left(\frac{||\mathbf{u}_p||}{\dot{\gamma}_r h_s}\right)^n. \tag{9}$$

The equation system (2)–(4) consists of five partial differential equations for the two scalar fields $h_p$, $h_s$ and the two 2-D vector fields $\mathbf{u}_p$, $\mathbf{u}_s$, which is equivalent to six scalar field variables. To close the system, we therefore need a further relation. In the 1-D case, one can impose $u_s = \alpha_1 u_p$ (Huang & García, 1997; Imran et al., 2001), ensuring continuity of the velocity across the layer interface and the steady state velocity profile in the shear layer. The analogous condition in 2HD, $\mathbf{u}_s = \alpha_1 \mathbf{u}_p$, represents two constraints and would overdetermine the system. Instead, we only demand

$$||\mathbf{u}_s|| = \alpha_1 ||\mathbf{u}_p||. \tag{10}$$

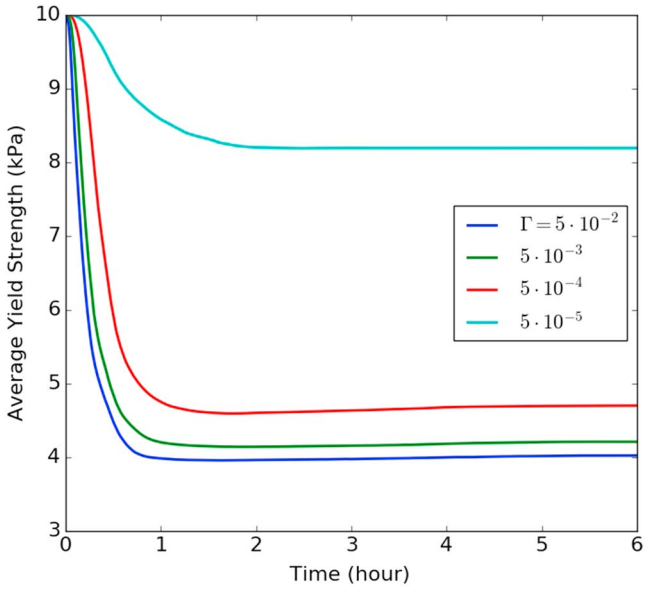


**Figure 2.** Spatially averaged yield strength versus time for different values of the remolding parameter $\Gamma$ in the case of simulations of the Storegga Slide with BingClaw. The initial yield strength is set to $\tau_{y,0} = 10\,\text{kPa}$.

From the computed values of $h \equiv h_p + h_s$, $h_p\mathbf{u}_p$ and $h_s\mathbf{u}_s$, we obtain $r \equiv \frac{h_s\|\mathbf{u}_s\|}{h_p\|\mathbf{u}_p\|} = \frac{\alpha_1 h_s}{h-h_s}$ and finally

$$h_s = h\frac{r}{\alpha_1 + r} \quad \text{and} \quad h_p = h\frac{\alpha_1}{\alpha_1 + r}. \tag{11}$$

Since $\alpha_1 > 0$ and $r \geq 0$, necessarily $h_s \geq 0$ and $h_p > 0$.

### 3.1.2. Remolding

De Blasio et al. (2005) proposed to approximate the effect of remolding or softening due to water intake by reducing the yield strength as a function of accumulated shear:

$$\tau_y(\gamma) = \tau_{y,\infty} + (\tau_{y,0} - \tau_{y,\infty})\mathrm{e}^{-\Gamma\gamma}, \tag{12}$$

where $\tau_{y,0}$ and $\tau_{y,\infty}$ are the initial and residual yield strength, respectively; $\gamma$ is the accumulated shear deformation at the bed; and $\Gamma$ is a dimensionless coefficient governing the rate of remolding. The remolding function (12) has been chosen on purely heuristic grounds as one of the simplest one-parameter functions with monotonic decrease.

The total shear strain at the bottom of the debris flow is calculated as

$$\begin{aligned}\gamma(\mathbf{x}(t), t) &= \int_0^t \|\partial_z \mathbf{u}(\mathbf{x}(t'), 0, t')\|\mathrm{d}t' \\ &= \frac{n+1}{n}\int_0^t \frac{\|\mathbf{u}_p(\mathbf{x}(t'), t')\|}{h_s(\mathbf{x}(t'), t')}\mathrm{d}t',\end{aligned} \tag{13}$$

where $\gamma$ is advected with the velocity $\mathbf{u}_s$. Note that the reference strain rate, $\dot{\gamma}_r$, and the flow exponent, $n$, are kept constant during remolding. This is equivalent to demanding that the shear-thinning behavior is unchanged, that the consistency $\mu$ decays at the same rate as the yield strength, and that the ratio of the initial and residual consistencies equals the ratio $\tau_{y,0}/\tau_{y,\infty}$. Our assumption that the flow exponent $n$ and the reference shear rate $\dot{\gamma}_r$ remain constant during remolding is merely for convenience and in the absence of experimental data. Small values of $\Gamma$ imply that large accumulated shear $\gamma$ is needed for remolding, and vice versa. It will be seen in section 4 that the early phase of the sliding process and tsunami genesis is sensitive to the value of $\Gamma$. Figure 2 plots the spatially averaged yield strength of Storegga Slide simulations with different values of $\Gamma$ as a function of time.

Including remolding in the model allows also for a gradual mass release, which mimics the retrogressive slide behavior that is captured in the more sophisticated landslide model of Gauer et al. (2005). This gradual release does not occur in simpler visco-plastic models without remolding such as BING (Imran et al., 2001), Volcflow (Kelfoun et al., 2010), and Geoflow-SPH (Pastor et al., 2009). In BingClaw, large parts of the release area with gentle slope and small earth-pressure gradients will be initially stable for sufficiently high values of $\tau_{y,0}$. If there is a slope break near the distal end of the release area or if the soil is partially remolded there, a small area may be unstable and start to slide. As the material flows out, the earth-pressure gradient at the newly formed headwall increases and destabilizes it, so that the failure propagates upslope. This property is favorable for modeling the Storegga landslide, which started with a toe-failure propagating up-slope. Even though BingClaw is not able to simulate the breakup into individual blocks that emerged in the depth-resolved simulations by Gauer et al. (2005), visual comparison of the two simulations suggests that the overall deformation pattern and the speed of the landslide, which are of importance for the tsunami generation, are nevertheless captured.

### 3.1.3. Hydrodynamic Drag

Following De Blasio et al. (2004), the hydrodynamic drag is split into the friction drag and pressure drag terms as $\tau_d = \tau_f + \tau_p$. The friction drag, $\tau_f$, is approximated as

$$\boldsymbol{\tau}_f = \frac{1}{2}C_F\rho_w\mathbf{u}_p\|\mathbf{u}_p\|, \tag{14}$$

and the pressure drag term, $\tau_p$, is modeled as

$$\boldsymbol{\tau}_p = \frac{1}{2}C_P\rho_w \max(0, -\mathbf{u}_p \cdot \nabla h)\mathbf{u}_p. \tag{15}$$

$\rho_w$ is the density of the ambient fluid, in the present case the density of sea water. Typical values of the form and pressure drag coefficients are $C_F = \mathcal{O}(10^{-2})$ and $C_P = \mathcal{O}(1)$. The term $\max(0, -\mathbf{u}_p \cdot \nabla h)$ ensures that the pressure drag acts only on portions of the slide facing in the forward direction. Neglecting suction due to vortex shedding in leeward areas and local differences in the flow velocity of the ambient fluid due to the nonuniformity of the slide surface, this is a simplistic approximation to the complex distribution of pressure drag along the surface of a moving irregular body. However, it captures the first-order effects of hydrodynamic drag and contributes greatly to keeping the simulated velocities in realistic bounds in very large slides (De Blasio et al., 2004).

#### 3.1.4. Added Mass

When a body is accelerated in a fluid, a considerable volume of fluid around the body also needs to be accelerated. This leads to additional transient forces on the body that, to first approximation, behave like inertial forces due to additional mass attached to the body. The force is proportional to the acceleration and volume of the body and the density of the ambient fluid, and it depends on the shape of the body and the immersion depth. It can be included in the momentum balance equations by multiplying the inertia terms (the time derivative and the advection term—the first two terms on the left-hand sides of equations (3) and (4)) by the factor $1 + C_M \rho_w / \rho_d$ (see, e.g., Grilli & Watts, 2005; Watts, 2000). There is no change to the mass balance equation. The added-mass coefficient $C_M$ for most bodies of reasonably compact shape is expected to be of order 1; however, the situation might be very different for slender slide bodies as discussed below.

Laboratory experiments by Watts (2000) using isosceles triangular wedges with a height-to-length ratio of about 0.7 on a 45° incline showed $C_M$ to vary in the range 0.5–1 in function of the ratio of submersion depth to body length. We note that other studies, namely, Enet and Grilli (2007) and Romano et al. (2016), derived experimentally added-mass coefficients in the lower end of this range, the latter study finding a value as low as 0.26. The deformability of the landslide mass may tend to minimize $C_M$ during the acceleration phase, but this is expected to be a minor effect. The added-mass coefficient can also be estimated analytically, as discussed by Enet and Grilli (2007), which would imply that the added-mass coefficient is proportional to the ratio between the slide thickness and the slide length. Enet and Grilli (2007) found that this factor of proportionality is 2.6, a factor of a similar order of magnitude might expected for Storegga. This might suggest that the added-mass coefficient will be low for the Storegga case, as the slide has a much longer length than thickness. For the Storegga slide, this ratio is $\mathcal{O}(10^{-3})$, so it is therefore doubtful that Watts' measurements for short blocks can be applied directly to the "slender" Storegga slide. On the other hand, the added mass is most important for tsunami genesis in the startup phase, which involves shorter horizontal length scales.

#### 3.1.5. Numerical Implementation

BingClaw combines a finite volume method with a finite difference method for the source terms. It builds on the GeoClaw variant (Berger et al., 2011) of the Clawpack library for solving conservation law equations (Clawpack Development Team, 2015; Mandli et al., 2016). Clawpack uses the Eulerian approach on structured meshes, combined with shock-capturing finite volume methods and Riemann solvers. GeoClaw is specialized to depth-averaged geophysical flows and featuring automatic mesh refinement; this is, however, disabled in BingClaw at present. As will be discussed shortly, one of the equations is not in conservation form; for this, the methods for general hyperbolic equations outlined in LeVeque (2002) are applied. The Clawpack library is also used in the two-phase granular landslide model D-Claw (George & Iverson, 2014).

One of the difficulties in the numerical implementation of the Herschel-Bulkley model arises from the momentum exchange terms $\pm\mathbf{u}_p[\partial_t h_s + \nabla\cdot(h_s\mathbf{u}_s)]$ in equations (3) and (4), which have been found to sometimes cause numerical instabilities. Here, we transform the equations in such a way that the momentum exchange term is implicitly included. First, we note that the momentum exchange terms cancel identically if the two equations are added to obtain the momentum balance equation for the entire flow. With $h \equiv h_p + h_s$ and $h\mathbf{u} \equiv h_p\mathbf{u}_p + h_s\mathbf{u}_s$, the new equation reads

$$\begin{aligned} &\partial_t(h\mathbf{u}) + \nabla\cdot[(h_p + \alpha_2 h_s)\mathbf{u}_p\mathbf{u}_p] + g' h \nabla(h + b) \\ &\quad = -\frac{\mathbf{u}_p}{\|\mathbf{u}_p\|}\frac{\tau_y}{\rho_d}(1 + f_s). \end{aligned} \tag{16}$$

Next we note that the mass exchange rate $q$ defined in section 3.1.1 is part of the mass balance equation (2) for the entire flow and can therefore be expressed in terms of $h_p$ and $\mathbf{u}_p$:

$$\partial_t h_s + \nabla \cdot (h_s \mathbf{u}_s) = -\partial_t h_p - \nabla \cdot (h_p \mathbf{u}_p).$$

Upon inserting this expression in equation (3) and dividing by $h_p$, we arrive at

$$\begin{aligned} \partial_t \mathbf{u}_p + \mathbf{u}_p \cdot \nabla \mathbf{u}_p + g' \nabla (h + b) \\ = -\frac{\mathbf{u}_p}{||\mathbf{u}_p||} \frac{\tau_y}{h_p \rho_d}. \end{aligned} \tag{17}$$

The mass balance equation (2) can immediately be rewritten in the variable $h\mathbf{u}$ as

$$\partial_t h + \nabla \cdot (h\mathbf{u}) = 0. \tag{18}$$

The new system contains the five equations (18), (16), and (17) with the seven unknowns $h$, $h_s$, $h_p$, $h\mathbf{u}$, and $\mathbf{u}_p$. The two algebraic constraints $h = h_s + h_p$ and $h\|\mathbf{u}\| = (h_p + \alpha_1 h_s)\|\mathbf{u}_p\|$ allow to close the system.

Our numerical scheme proceeds in three steps at each time step. First, the earth-pressure gradient combined with gravity, $\rho_d g' h \nabla (h + b)$, is compared to the yield strength ($\tau_y$) at each cell $(i,j)$ where the material is at rest. If the yield strength is larger than the driving forces in a computational cell, then this cell is stable, and no motion is imposed. If two adjacent cells are stable, there is no flux at their interface, and the following steps are not necessary. If at least one of the cells is unstable or in motion, we proceed to the following steps. Second, the set of equations without friction terms is solved for the time step from $t_{n-1}$ to $t_n$. At each cell interface, we solve a Riemann problem with the wave propagation algorithm of the finite volume method (LeVeque, 2002) and obtain the predictor step at time $t_n$, that is, $h^{(n)}$, $\tilde{h}_p^{(n)}$, $\widetilde{h\mathbf{u}}^{(n)}$, $\tilde{\mathbf{u}}_p^{(n)}$ (the provisional solution for the total flow depth coincides with the complete solution). The final step is to apply the friction forces to the intermediate solution using a Godunov fractional step method:

$$\partial_t \tilde{\mathbf{u}}_p = -\frac{\tilde{\mathbf{u}}_p}{\|\tilde{\mathbf{u}}_p\|} \frac{\tau_y}{h_p \rho_d} - \frac{\tau_p + \tau_d}{h_p \rho_d}, \tag{19}$$

$$\partial_t (h\tilde{\mathbf{u}}) = -\frac{\tilde{\mathbf{u}}_p}{\|\tilde{\mathbf{u}}_p\|} \frac{\tau_y}{\rho_d} (1 + f_s). \tag{20}$$

Equation (17) is not in conservation form and therefore deserves a separate discussion. As explained, for example, in LeVeque (2002, chapters 16.5 and 16.6), the finite volume technique can be applied to nonconservative equations as well, provided the correct wave propagation speeds can be determined. This has later been confirmed by other independent studies, (e.g., Castro et al., 2008), indicating that a conservation form of the equation is not a necessary condition for using Riemann solvers. The main problem, however, is to find the correct wave propagation velocities. In the case at hand, the system is a rather special two-layer flow in that the two layers consist of the same material and the interface between them is not material. It can be shown (Issler, 2010) that the balance equations can be rewritten in terms of the balance of total mass (18), total momentum (20), and an evolution equation for the ratio $r \equiv h_s/h$. The latter is not a conservation equation, but its physical interpretation implies that discontinuities in $q$ must be accompanied by jumps in $\mathbf{u}$ and $h$ because a jump only in $q$ would not conserve mass and momentum. This means that shocks in $q$ propagate at the same speed as shocks in $h$ and $\mathbf{u}$. In this way, the wave speeds in the Riemann problem can be determined.

### 3.2. Landslide-Tsunami Coupling and Tsunami Propagation Modeling

The motion of the submarine landslide and the tsunami propagation is coupled in a one-way scheme; that is, the wave is generated by the change of the bottom bathymetry while the effect of the sea surface change on the landslide motion is neglected. The landslide-tsunami generation and propagation are simulated combining BingClaw and the Boussinesq-type tsunami model BoussClaw (Kim et al., 2017) for the respective visco-plastic landslide and tsunami generation. It turned out that frequency dispersion was negligible and that the shallow-water equations were adequate for simulating the wave propagation. For each time step, we copy the change of water depth due to the landslide progression as changes to the water surface height. In

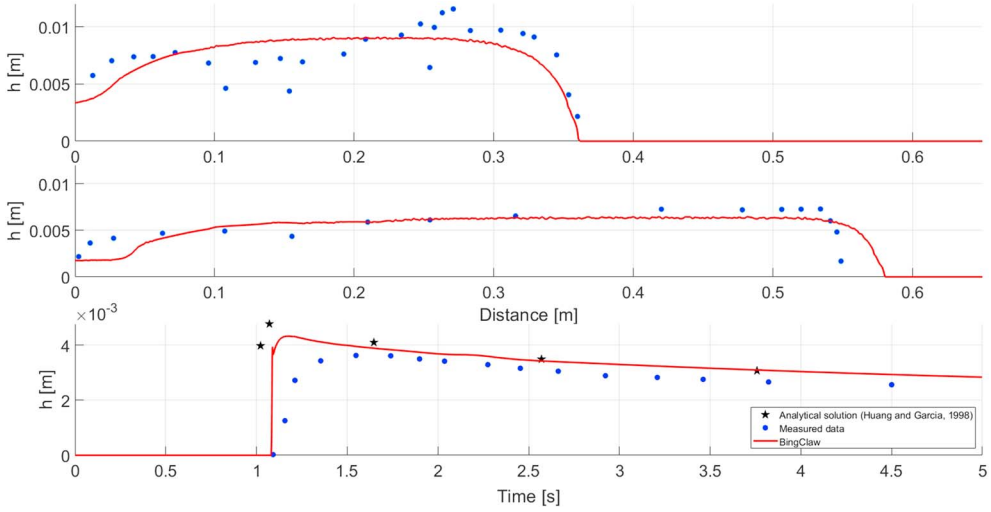


**Figure 3.** Comparison between experimental data and analytical solution from Huang and García (1998) with numerical simulations using BingClaw. Upper panel, final flow deposit for $\tau = 14.1$ Pa, $\mu = 10.2\,\mathrm{N\,m^{-2}\,s^{n}}$, and $n = 0.34$. Middle panel, final flow deposit for $\tau = 10.0$ Pa, $\mu = 7.1\,\mathrm{N\,m^{-2}\,s^{n}}$, and $n = 0.38$. Lower panel, evolution of landslide thickness at $x = 0.689$ m for $\tau = 2.21$ Pa, $\mu = 0.22\,\mathrm{N\,m^{-2}\,s^{n}}$, and $n = 0.75$.

other words, the change in water surface due to nonhydrostatic pressure as in Kajiura (1963) is not accounted for (see Løvholt et al., 2015, for a discussion). In the present example we could do this because the slow modulation of the landslide speed combined with its large size produced long waves.

## 4. Results

### 4.1. Validation Against Experimental Data

Huang and García (1998) conducted a set of experiments in the laboratory for clay-water mixtures with carefully measured rheological properties. The fluid mixture was initially contained behind a sliding gate distributed over 10 cm in the dip direction (measured along the sloping plane). Their experiments were conducted by letting the clay-water mixture flow in a plexiglas tank that can be tilted at an arbitrary angle. The width of the plexiglas tank was 30 cm, which was sufficient for the flow to be mainly one-dimensional (i.e., characterized by uniform downslope motion). The experiments were conducted for different material properties. In addition to the experimental work, Huang and García (1998) also developed asymptotic solutions for the development of the landslide thickness in idealized geometries. These experiments and the asymptotic solutions allow us to test how the landslide model can reproduce landslides in a well-controlled environment. However, they cannot be used for describing more complex behavior, such as remolding and influence of the topography on the dynamics.

Here, we use BingClaw to simulate three different cases presented by Huang and García (1998):

- A flow of a relatively stiff and viscous slurry with $\tau = 14.1$ Pa, $\rho = 1{,}348\,\mathrm{kg/m^3}$, $\mu = 10.2\,\mathrm{N/m^2\,s^{n}}$, and $n = 0.34$. The slope angle was $\theta = 18.5°$. Huang and García (1998) reported an initial landslide area of 29.2 $\dot{\mathrm{c}}\mathrm{m}^2$, but integrating their reported slide thickness, we found that the area was smaller by a factor 0.91 than the one they reported. We conjecture that this could be due to adhesion of the slurry to the wall. We used this factor to correct the initial area. We then distributed the initial landslide volume behind the sliding gate, an initial height of $h_0 = 2.79$ cm providing a slide area that matched the observed area derived from the laboratory results.
- A flow of more liquid, softer material with $\tau = 10.0$ Pa, $\rho = 1{,}323\,\mathrm{kg/m^3}$, $\mu = 7.1\,\mathrm{N/m^2\,s^{n}}$, $n = 0.38$. The slope angle was $\theta = 24.5°$. Huang and García (1998) reported an initial landslide area of 32.4 $\mathrm{cm}^2$, but integrating their reported slide thickness, we found that the area was a factor 0.92 lower than the one they reported. We used this factor to correct the initial area. We then distributed the initial landslide volume behind the sliding gate, a height of $h_0 = 3.1$ cm provided a slide area that complied with the observed area derived from the laboratory results.

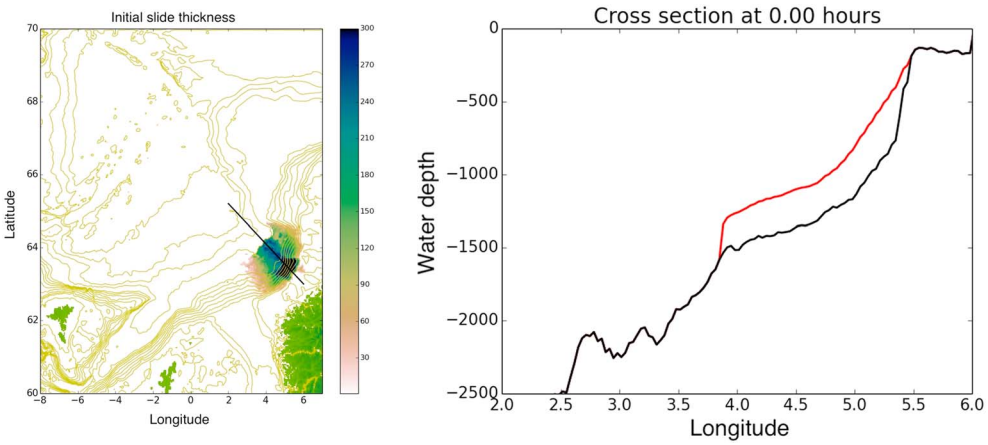


**Figure 4.** Assumed initial shape of the Storegga Slide simulations with BingClaw: release height distribution (left panel) and longitudinal section (right panel ) along the black line in the left panel.

- A very soft material with the parameters $\tau = 2.21$ Pa, $\rho = 1{,}315\,\mathrm{kg/m^3}$, $\mu = 0.22\,\mathrm{N/m^2\,s^n}$, $n = 0.75$. The slope angle was $\theta = 11°$, and the initial landslide thickness $h_0 = 2.26$ cm. As the deposit thickness as a function of $x$ is not shown in Huang and García (1998) in this case, we did not apply any volume correction.

The simulations were conducted for a 1-cm-wide strip of the original experiments with reflecting side boundaries, that is, assuming uniform flow downslope. Inspection of images displayed by Huang and García (1998) may suggest that this assumption might be slightly violated in their experiments. A grid resolution of 1 mm × 1 mm (measured horizontally) was used. Remolding, hydrodynamic drag, and added-mass effects were turned off in the simulations. Comparisons between the simulations and experiments for the slide thickness at the final runout distance are shown in the upper and mid panels of Figure 3. Good agreement between the measurements and the simulations was obtained, particularly for the first case, while the runout is slightly too long in the second example. We emphasize that our input parameters were identical to those measured by Huang and García (1998) with no attempt to tune the parameters apart from the area corrections. The lower panel of Figure 3 compares the simulated landslide thickness at a distance 0.689 m downstream of the sliding door to both the asymptotic solution and the experimental results for the softest test case. As shown, we obtain close agreement with the asymptotic solution shortly after the mixture has passed the gauge. Further, we show that both the model and the asymptotic solution reach slightly higher velocities than the experimental flow. The agreement between the asymptotic solution and our new numerical model shows that the latter gives results that are consistent with the asymptotic formulation derived by Huang and García (1998).

### 4.2. Derivation of Plausible Landslide Parameter Ranges by Comparing Simulations With Runout Observations

The initial shape of the Storegga Slide is reconstructed based on the study of Bryn et al. (2005). The maximum release depth is about 450 m, and the released volume is 3,500 km$^3$ (this was chosen about 10% larger than the upper limit quoted by Haflidason et al., 2004, because a part of the potential landslide volume was not mobilized in the simulations). Figure 4 shows the spatial distribution of release height and the release height along a transect.

Landslide parameters at the time of the release of the Storegga Slide cannot be precisely known, first owing to the expected spatial variability of the slide masses (the slide area is vast and soil properties are only measured in a few locations), changes in soil properties since the time of release, and lack of ability to measure

**Table 1**
*Fixed Parameters for the Visco-Plastic Landslide Simulations*

| $\dot{\gamma}_r$ | $n$ | $\rho_a$ | $\rho_d$ | $C_F$ | $C_P$ |
|---|---|---|---|---|---|
| $\mathrm{s^{-1}}$ | — | $\mathrm{kg/m^3}$ | $\mathrm{kg/m^3}$ | — | — |
| 100 | 0.5 | 1,000 | 1,860 | 0.01 | 1 |

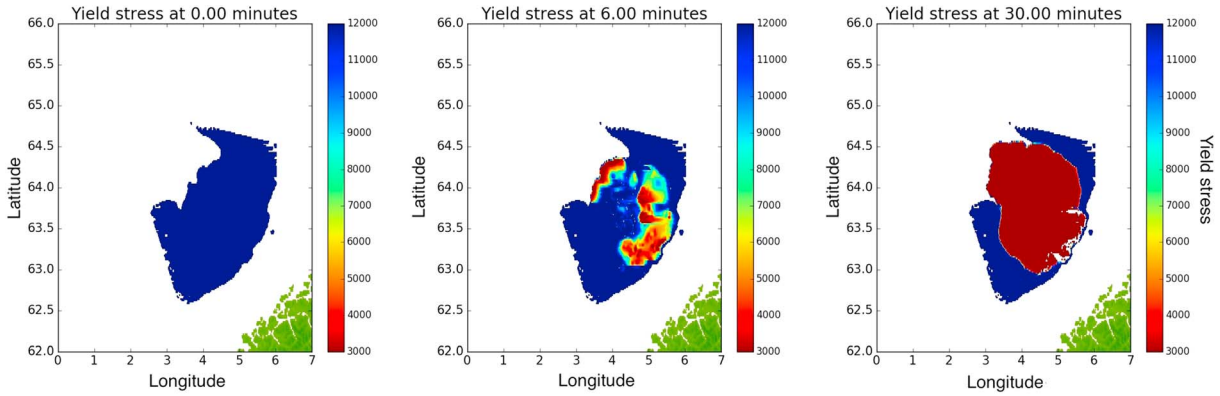


**Figure 5.** Plot of the yield stress $\tau_y(\gamma)$ with remolding at $t = 0$, 6, and 30 min for the case $\tau_{y,0} = 12$ kPa, $\tau_{y,\infty} = 3$ kPa, and $\Gamma = 5 \times 10^{-3}$.

secondary properties such as remolding and erosion. For this reason, we do not attempt to model the slide using material parameters measured on samples (there were no consistent measurements available anyway) but conduct a parameter study spanning the range of material properties we consider realistic. Note that the mass mobilized in the Storegga Slide is rather inhomogeneous, including overconsolidated glacio-marine clays as well as underconsolidated, overpressurized ooze. Furthermore, consolidation implies that the soil was softer at the time of the slide release than it is today.

The value of the initial yield strength is limited by the fact that the Herschel-Bulkley model allows initiation of slide motion only where the combination of the earth-pressure gradient and gravity integrated over a columnar volume element is larger than the yield strength integrated over the base of the column, as explained in section 3.1.5. We tested the $4^3 = 64$ parameter sets $\{\tau_{y,0}, \tau_{y,\infty}, \Gamma\}$ obtained from $\tau_{y,0} \in \{7, 10, 12, 15\}$ kPa, $\tau_{y,\infty} \in \{1, 2, 3, 3.5\}$ kPa, and $\Gamma \in \{5 \times 10^{-2}, 5 \times 10^{-3}, 5 \times 10^{-4}, 5 \times 10^{-5}\}$ because we expected tsunami generation to vary most strongly for these parameters and value ranges, and because they enable us to cover a reasonable landslide runout range. The remaining parameters were kept fixed at the values shown in Table 1. The assumed soil sensitivity (i.e. ,$\tau_{y,0}/\tau_{y,\infty}$) of the slide material thus ranges from 2 to 15. We ran the simulations with these parameter combinations without including the effect of added mass, that is, $C_m = 0$. Some simulations addressing the effect of nonzero $C_m$ (for $C_m = 0.1$, 0.3, and 0.5) are briefly discussed below, but simulation results are not shown. In the simulations with nonzero

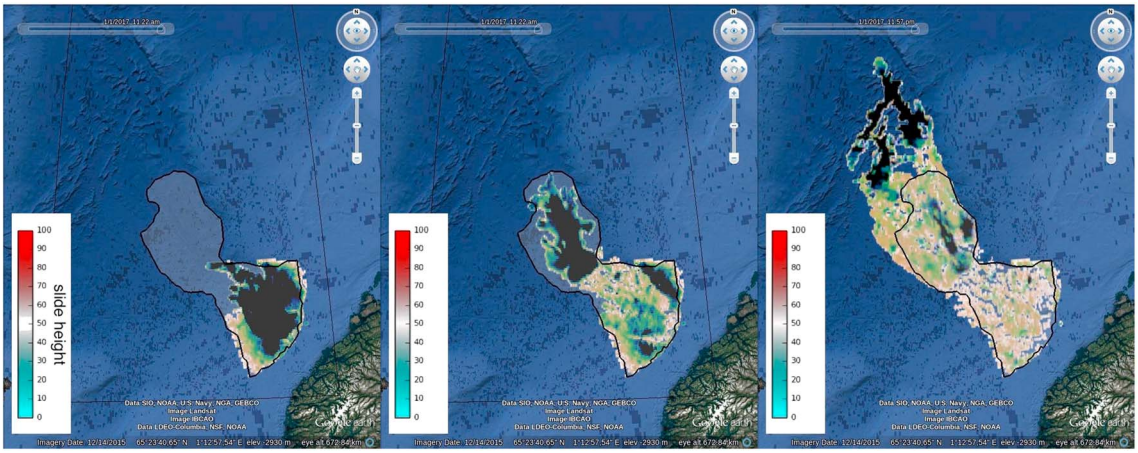


**Figure 6.** Final runout of the Storegga slide for three cases, simulated with BingClaw: $(\tau_{y,0}, \tau_{y,\infty}, \Gamma) = (15\,\text{kPa}, 3.5\,\text{kPa}, 5 \times 10^{-5})$, $(12\,\text{kPa}, 3\,\text{kPa}, 5 \times 10^{-4})$, and $(7\,\text{kPa}, 1\,\text{kPa}, 5 \times 10^{-2})$ (from left to right). The deposit inferred from the bathymetric analysis is indicated by the black line.

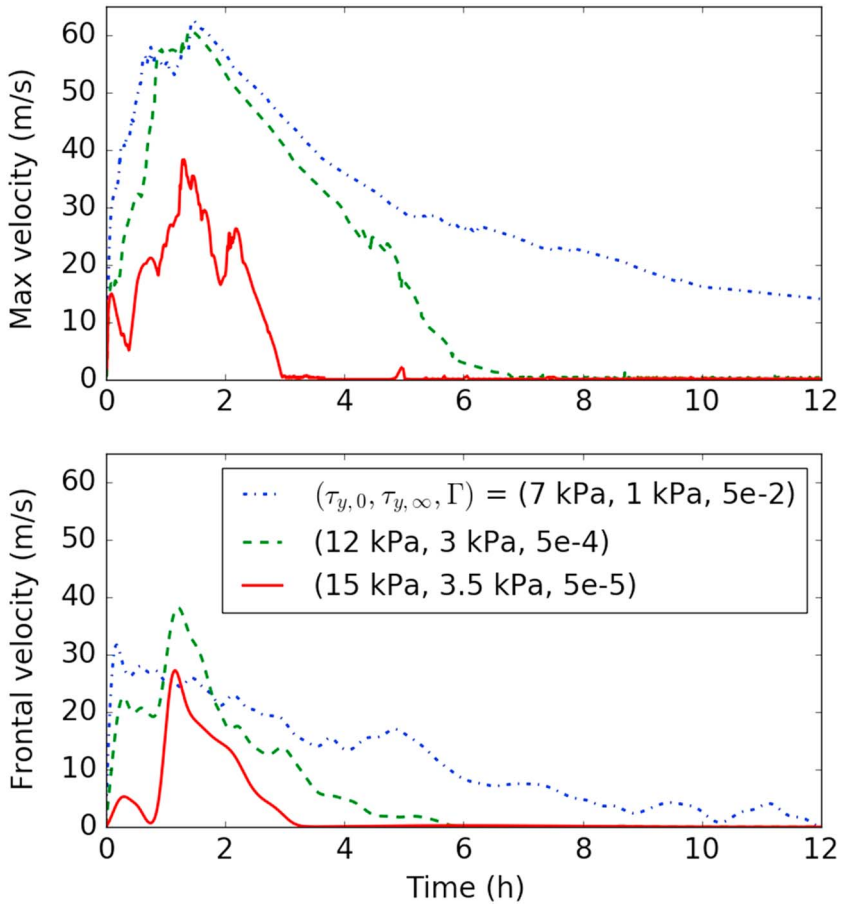


**Figure 7.** Maximum (top) and frontal progression velocity (lower panel) simulated with BingClaw for the example cases 1–3.

$C_m$, the yield strength parameters were set to lower values ($\tau_{y,0} = 8$ kPa, $\tau_{y,\infty} = 3$ kPa, and $\Gamma = 5 \times 10^{-3}$). The lower yield strength values imply lower shear-layer flow resistance.

Figure 5 illustrates the initiation of the landslide flow subject to remolding, showing the spatial distribution of the yield stress at $t = 0$, 6, and 30 min. Initially, the yield strength is $\tau_y = \tau_{y,0} = 12$ kPa throughout the release mass in this simulation. In the beginning, only the slightly steeper areas at the front and upper reaches of the center of the release area start moving. As shear accumulates in the moving areas, $\tau_y$ decreases there, and thus, the acceleration increases. With the mass flowing out from the center area, the failure spreads sideways. At $t = 6$ min, $\tau_y$ has decreased close to the fully remolded value (set to $\tau_{y,\infty} = 3$ kPa in this simulation) in the upper reaches and at the front of the flow, and after 30 min most of the landslide volume is fully remolded.

To demonstrate the wide range of slide behavior, we focus on three parameter combinations that span the landslide and tsunami behavior out of the 64 cases, labeled cases 1–3:

- Case 1: landslide with high initial shear strength, moderate sensitivity, and slow remolding: $\tau_{y,0} = 15$ kPa, $\tau_{y,\infty} = 3.5$ kPa, and $\Gamma = 5 \times 10^{-5}$.
- Case 2: landslide with intermediate initial shear strength, moderate sensitivity, and intermediate remolding speed: $\tau_{y,0} = 12$ kPa, $\tau_{y,\infty} = 3$ kPa, and $\Gamma = 5 \times 10^{-4}$. This parameter combination will be seen below to be favorable with respect to both the paleo-tsunami observations and the landslide runout distance, providing smaller overall error norms than the other examples.
- Case 3: landslide with low initial shear strength, high sensitivity, and rapid remolding: $\tau_{y,0} = 7$ kPa, $\tau_{y,\infty} = 1$ kPa, and $\Gamma = 5 \times 10^{-2}$.

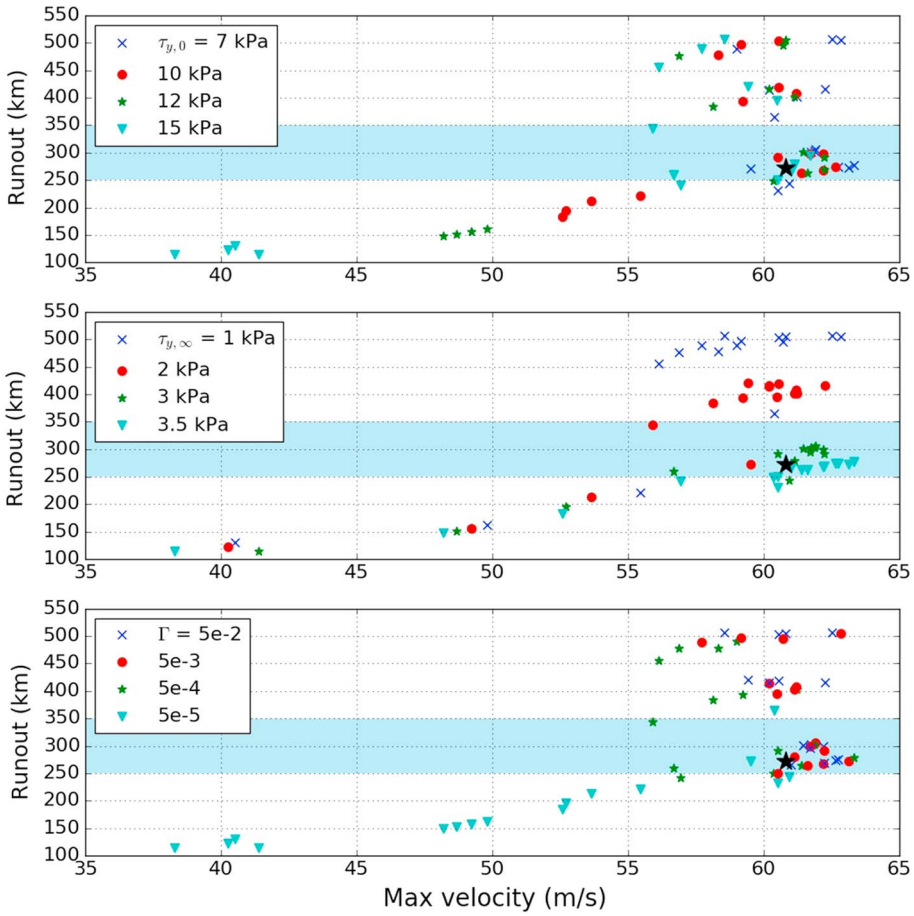


**Figure 8.** Runout distance as a function of the maximum velocity. The blue-shaded region ranging from 250 to 350 km comprises the observed runout distance (measured from the toe of the release area, about 100 km from the headwall). The black star (⋆) identifies the best fit for the joint landslide-tsunami model, $(\tau_{y,0}, \tau_{y,\infty}, \Gamma) = (12\,\text{kPa}, 3\,\text{kPa}, 5 \times 10^{-4})$.

In Figure 6, the simulated slide deposits are compared with the observed runout (Haflidason et al., 2004) of the debris flow for the three different parameter combinations. With low yield strength, high sensitivity and rapid remolding (case 3), more or less all the mass escapes the slide escarpment. The movement of the slide stops completely after about 40 hr, and the simulated runout is about 150 km too long. The opposite effect is observed for case 1 where only a small fraction of the landslide is mobilized. The runout is too short by approximately 150 km, and the landslide movement almost stops already after 2.5 hr. A rather favorable comparison is, however, obtained for case 2 with the parameter combination $(\tau_{y,0}, \tau_{y,\infty}, \Gamma) = (12\,\text{kPa}, 3\,\text{kPa}, 5 \times 10^{-4})$. In this case, the runout distance is very well matched, whereas the lateral spreading falls somewhat short of the observations (however, the bathymetric measurements available for the morphological analysis are much less dense in the distal region of the deposit, which may account for some of the discrepancy). We further note that the shape of the thickest part of the deposit also matches the second largest lobe structures identified by Haflidason et al. (2005).

In Figure 7, the maximum and frontal progression velocity are shown as a function of time for cases 1–3. The maximum velocity represents the maximum value of the slide speed over the entire flow domain at a given time, and the frontal progression velocity is deduced from the front location. For case 2, the maximum velocity peaks at about 60 m/s after 1.5 hr, which is similar to the numerical results of De Blasio et al. (2004). At all times, the frontal progression velocity is significantly smaller than the maximum internal velocity. For the same parameter combination, the frontal progression velocity peaks at 40 m/s. The frontal progression velocity is nevertheless considerably larger than the block velocities of 20–35 m/s used in previous hindcasts

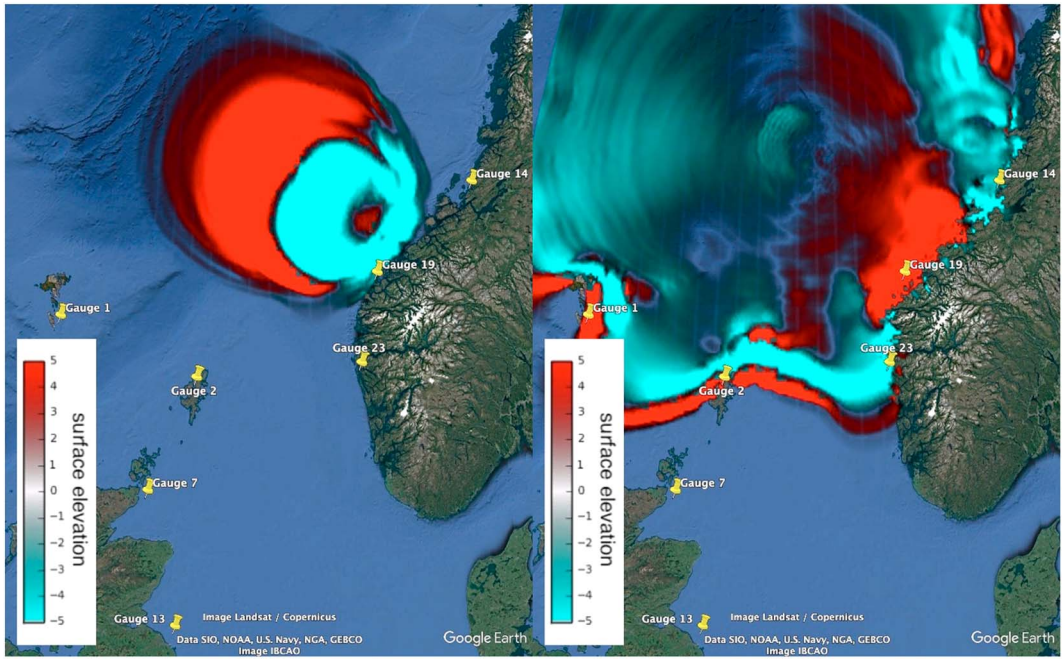


**Figure 9.** Snapshots of the simulated Storegga tsunami at $t = 40$ min and $t = 2$ hr. The tsunami is generated by the landslide simulation with BingClaw using the parameter set $(\tau_{y,0}, \tau_{y,\infty}, \Gamma) = (12\,\text{kPa}, 3\,\text{kPa}, 5 \times 10^{-4})$.

of the Storegga tsunami (Bondevik et al., 2005). From the velocity profiles in Figure 7, one also infers much higher accelerations than obtained by Bondevik et al. (2005), particularly for the case with low yield strength.

Figure 8 plots the maximum velocities and runout distances for all 64 landslide simulations, with the blue-shaded region between 250 and 350 km runout distance comprising simulations with reasonably realistic results. Note that the runout distance here is measured from the toe of the release area, which is a little more than 100 km downslope from the headwall. Within the tested parameter range, the simulated runout distances form different clusters around 300, 400, and 500 km or fall into the range 100–250 km. We furthermore note the following points:

- The scenarios that fall within the plausible observation range provide a range of maximum velocities from about 55–63 m/s. Different parameter combinations fit within this observation window.
- The remolded yield strength $\tau_{y,\infty}$ has the strongest influence on the landslide runout distance, and most of the remolded yield strength values in the observation window range between 3 and 3.5 kPa.
- The largest values of the remolding coefficient $\Gamma$, that is, $5 \times 10^{-2}$–$5 \times 10^{-3}$, provide the highest relative number of scenarios within the runout observation window. The scenarios with lower values of $\Gamma = 5 \times 10^{-5}$ mostly fall outside the runout observation window.
- $\Gamma$ has a strong influence on the maximum slide velocity. As shown in Figure 8, with $\Gamma \geq 5 \times 10^{-4}$, all slides attain a peak velocity of 56–63 m/s, whereas those with $\Gamma = 5 \times 10^{-5}$ peak at less than 50 m/s unless $\tau_{y,0} \leq 10$ kPa.
- The maximum runout distance is much less sensitive to the initial yield strength $\tau_{y,0}$ than to the two other parameters. However, $\tau_{y,0}$ influences the maximum velocity.
- The longest runout distances are also limited by topographic features. In particular, the Ægir Ridge located on the deep abyssal plain limits the runout distance to 500 km.

### 4.3. Optimizing Landslide Parameters Based on Tsunami Simulations and Paleo-Tsunami Observations

The landslide-generated tsunamis are simulated with the numerical scheme that is discussed in section 3.2. We simulated the wave propagation using the paleo-bathymetry reconstructed by Hill et al. (2014). Adaptive grid refinement is applied, with the finest grid size being equal to $1'$. Because the waves are extremely long compared to the water depth, they do not amplify significantly from the open sea to our selected points on the shoreline so that we can use the maximum tsunami heights from the offshore tsunami simulations to esti-

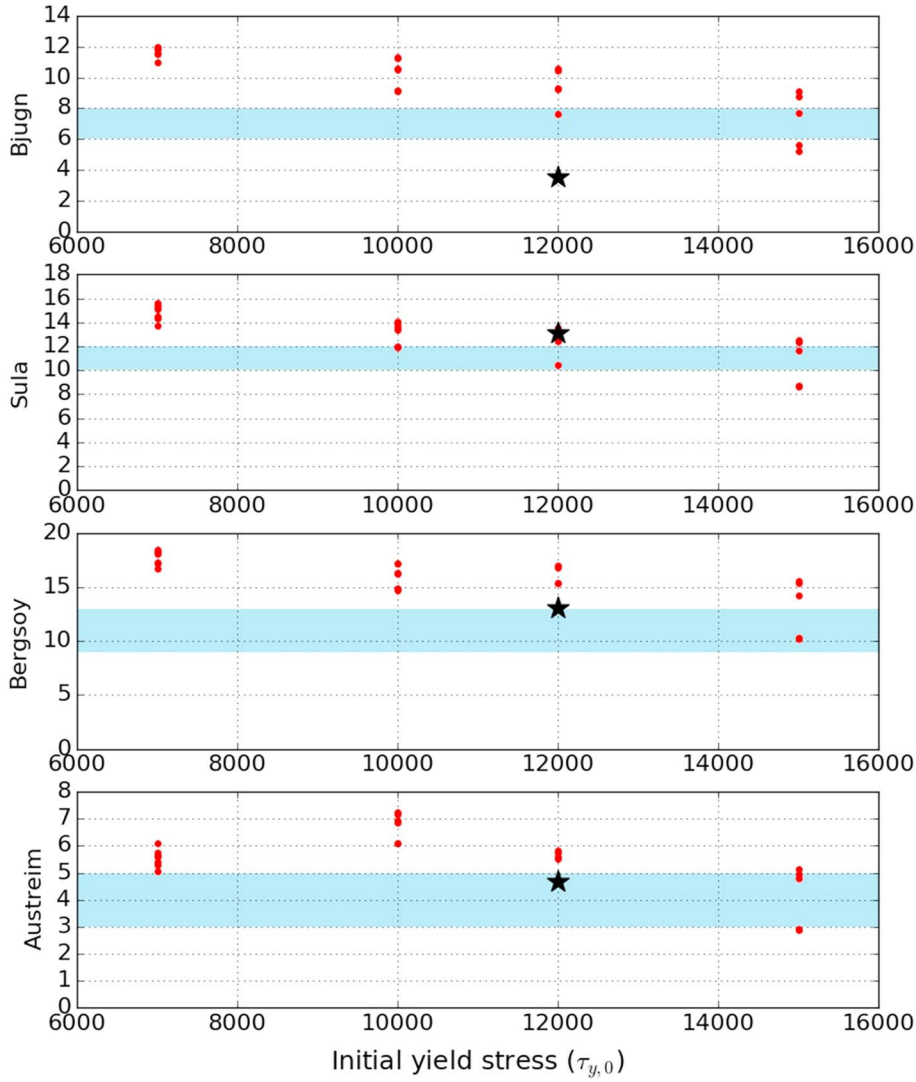


**Figure 10.** Maximum tsunami height at four locations on the Norwegian coast for 20 simulations simulated with BingClaw and resulting in runout distances between 250 and 350 km. The blue-shaded horizontal strips represent the field observations, and the black asterisk (⋆) identifies the best fit simulation for the joint landslide-tsunami model with $(\tau_{y,0}, \tau_{y,\infty}, \Gamma) = (12\,\text{kPa}, 3\,\text{kPa}, 5 \times 10^{-4})$.

mate paleo-tsunami runup. This was confirmed by an independent, more detailed analysis of the tsunami runup at some of the sites along the Norwegian coast (Løvholt et al., 2017), and also used previous simulations of the event (Bondevik et al., 2005; Harbitz, 1992). Time series of water surface elevation at control points ("gauges") were extracted from the tsunami simulations. The gauges correspond to the paleo-tsunami observations summarized in (Bondevik et al., 2005); they are indicated in Figure 9 together with snapshots of the simulated best-fit tsunami after 40 min and 2 hr. The far-field gauges 1, 2, 7, and 13 are located on the shore of the Faroe Islands, Shetland Islands, northern Scotland, and northeastern Scotland, respectively. The near-field gauges 14, 18, 19, and 23 represent Bjugn, Sula, Bergsøy, and Austreim on the Norwegian coast.

Among the 64 simulations, we have chosen 20 cases whose runout distances are within generous limits around the observed runout, that is, within 250–350 km from the toe of the release area, as shown in Figure 8. For the simulated tsunami water heights from these 20 cases, see Figures 10 and 11. Most of the simulations generate somewhat too high tsunamis in the near-field at Bjugn, Sula, Bergsøy, and Austreim on the Norwegian coast, but the best-fit parameter set matches the near-field observations rather well. The simulated tsunami water heights at the four selected far-field locations (Faroe Islands, Shetland Islands, and northern and northeastern Scotland) spread more evenly around the observed values (Figure 11). At the Shetland

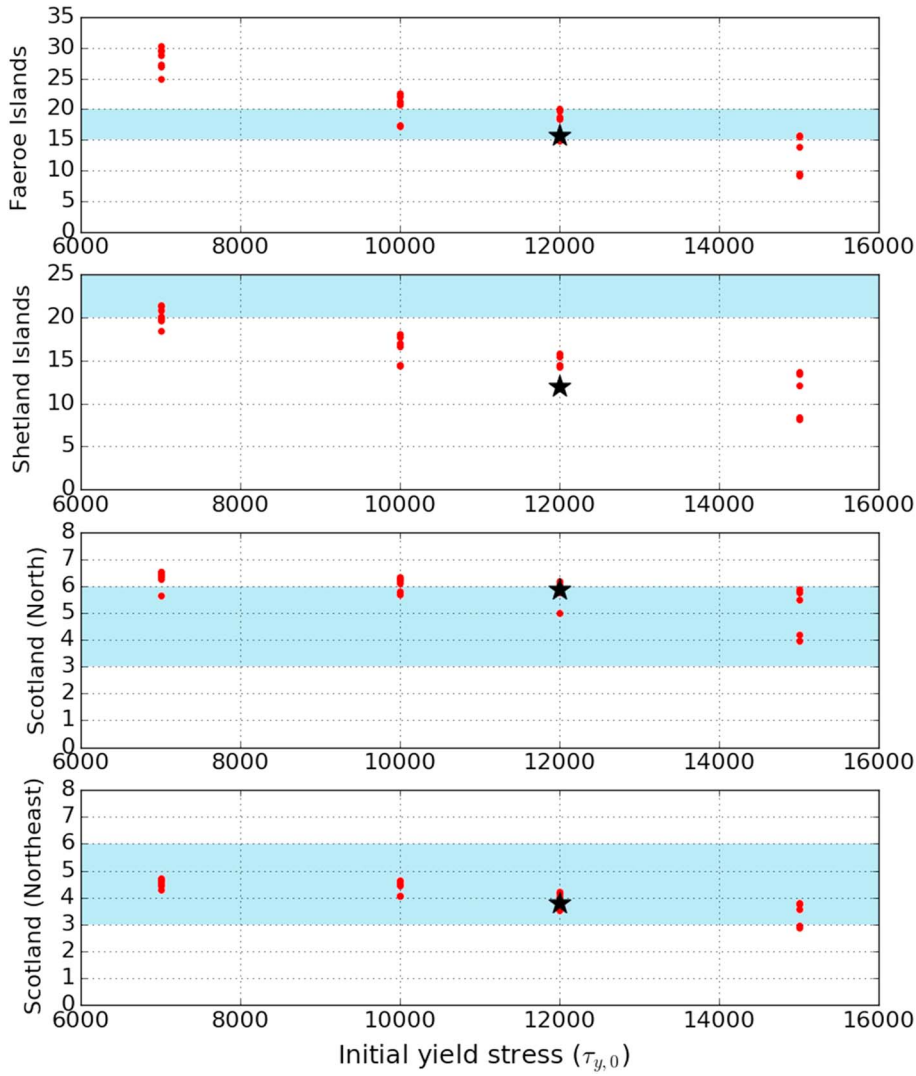


**Figure 11.** Maximum tsunami height at four far-field locations for 20 simulations with BingClaw that resulted in runout distances between 250 and 350 km. The blue-shaded horizontal strips represent the field observations, and the black asterisk (⋆) identifies the best fit simulation for the joint landslide-tsunami model with $(\tau_{y,0}, \tau_{y,\infty}, \Gamma) = (12\,\text{kPa}, 3\,\text{kPa}, 5 \times 10^{-4})$.

Islands, virtually all simulations (including the best-fit simulation) fall significantly short of the rather high observed value of 20–25 m. This singular disagreement suggests that some local bathymetric features that are not captured in our seafloor model might be important in this case. Alternatively, this might indicate that the assumed prehistoric sea level at 8,100 BP is not correct at this location.

To determine quantitatively how well the simulations compare with the observations, we define a dimensionless simulation error by

$$\text{Error} = \left[\frac{1}{N}\sum\left(\frac{\eta_{\text{num}} - \eta_{\text{obs}}}{\eta_{\text{obs}}}\right)^2\right]^{1/2}, \tag{21}$$

where $\eta_{\text{num}}$ and $\eta_{\text{obs}}$ are the computed tsunami water heights and observed paleo-tsunami heights, respectively, and $N$ is the number of gauges. The scenario that provided the smallest error norm is depicted by a black asterisk in Figures 10–12 and shown as a function of the initial yield strength $\tau_{y,0}$. This scenario compares well with five of the investigated locations; the sites offshore Norway inherit small deviations, whereas a discrepancy of almost 10 m from the observations is found at Shetland Islands, which makes this location anomalous. Taking only the far-field observations, the smallest error is found for $(\tau_{y,0}, \tau_{y,\infty}, \Gamma) = (10\,\text{kPa},$

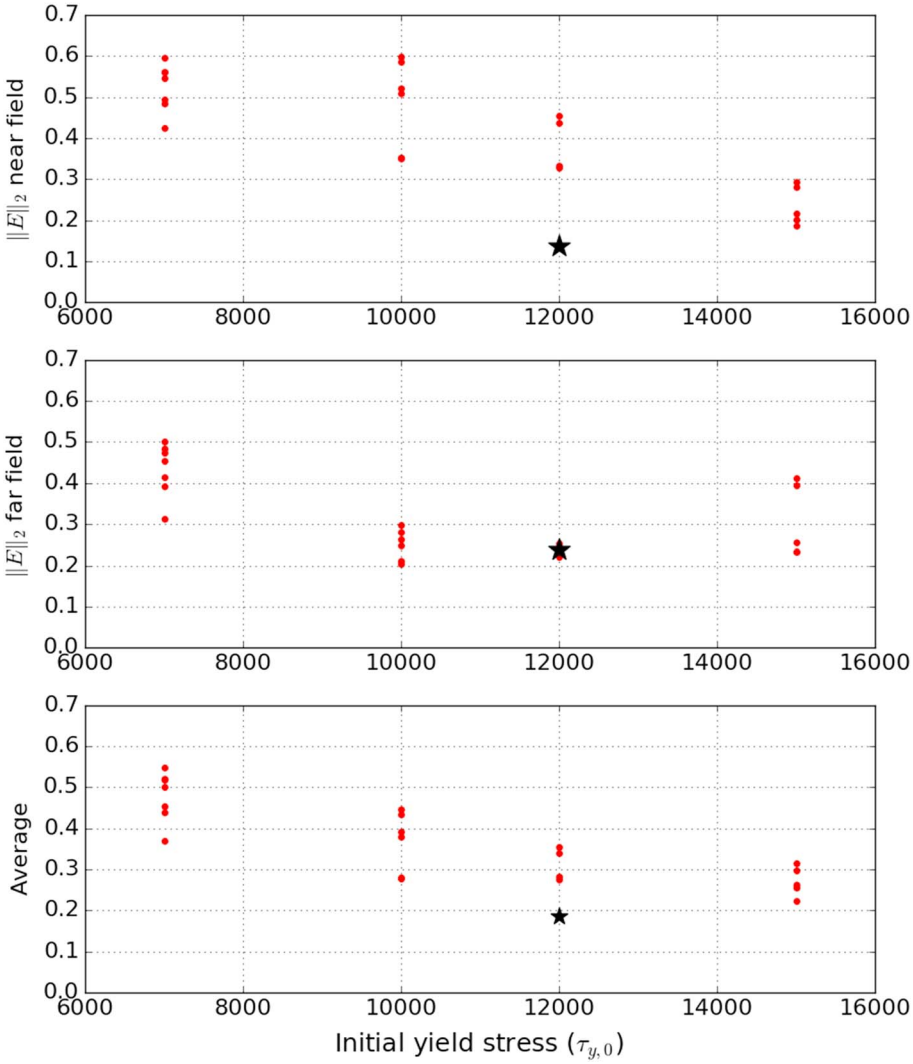


**Figure 12.** Combined runup errors at the near-field and far-field locations as a function of the initial yield strength, $\tau_{y,0}$. Among the 64 simulations, 20 cases are chosen whose runout distance falls into the range 250–350 km. The black asterisk ($\star$) indicates the best fit, $(\tau_{y,0}, \tau_{y,\infty}, \Gamma) = (12\,\text{kPa}, 3\,\text{kPa}, 5 \cdot 10^{-4})$.

3.5 kPa, $5{\times}10^{-4}$), whereas case 2 (12 kPa, 3 kPa, $5{\times}10^{-4}$) minimizes the error for all locations taken together.

We investigate the sensitivity to the different parameters by choosing a reference point in parameter space, $\mathbf{P}_{\text{ref}}$, and calculating the ratio of the relative change of some output variable, $\Delta R_i/R_{i,\text{ref}}$, and the relative change of a parameter value, $\Delta P_j/P_{j,\text{ref}}$:

$$S_{ij} \equiv \frac{\Delta R_i/R_{i,\text{ref}}}{\Delta P_j/P_{j,\text{ref}}}. \tag{22}$$

Here, we vary $(\tau_{y,0}, \tau_{y,\infty}, \Gamma)$ and choose the reference point as $\mathbf{P}_{\text{ref}} = (\tau_{y,0}, \tau_{y,\infty}, \Gamma)_{\text{ref}} = (12\,\text{kPa}, 3\,\text{kPa}, 5{\times}10^{-4})$. More precisely, instead of $\Gamma$ we use $-\log\Gamma$ because $\Gamma$ appears in the exponent of an exponential function. Representative sensitivity plots are shown in Figure 13 for the landslide runout distance and in Figure 14 for the maximum tsunami heights at the Faroe Islands and at Sula in Norway.

The runout distance is moderately sensitive to changes in $\tau_{y,0}$, but about twice as sensitive to changes in $\tau_{y,\infty}$. The sensitivity of the runout distance to the remolding parameter is clearly nonlinear and becomes pronounced for $\Gamma < \Gamma_{\text{ref}} = 5 \times 10^{-4}$ in the particular setting of the Storegga slide. Indeed, if $\tau_{y,0} = 12\,\text{kPa}$, $\tau_{y,\infty} = 3\,\text{kPa}, \Gamma = 5 \times 10^{-5}$ (the right-most red point in Figure 13), only a limited part of the landslide mass is mobilized and the final deposit looks similar to the left-most panel of Figure 6. This indicates that if the

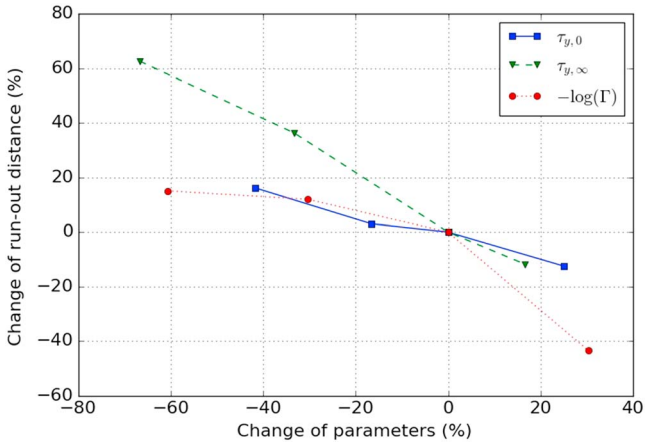


**Figure 13.** Parameter sensitivity tests for runout distance. Change of runout distance is shown with respect to the change of parameters. Parameter changes are relative to $\tau_{y,0} = 12\,\text{kPa}$, $\tau_{y,\infty} = 3\,\text{kPa}$, and $\Gamma = 5 \times 10^{-4}$. The runout distance is most sensitive to changes in $\tau_{y,\infty}$.

rate of remolding is too low, the yield strength does not reach sufficiently small values to allow the slide to flow farther along the extremely gentle slope of the abyssal plain.

The maximum tsunami height in the near-field and even more so in the far-field is highly sensitive to changes in the initial yield strength, but almost independent of the remolded yield strength (Figure 14). The $\Gamma$ factor also influences the tsunami generation significantly. As for the runout distance, the sensitivity to the value of $-\log\Gamma$ is strongly nonlinear, with $\Gamma \approx 5 \times 10^{-4}$ again marking the transition from strong to weak dependence.

The different sensitivities of the slide runout distance and the maximum tsunami height reflect the different phases of the landslide that control the different aspects of the flow after failure. The runout distance is mainly determined by the resistance at the bed, that is, by the value of $\tau_{y,\infty}$ and to a lesser degree by the value of the reference strain rate, $\dot{\gamma}_r$ (hydrodynamic drag becomes increasingly unimportant at low velocity, i.e., a long time after failure). If the slope angle decreases monotonically with distance from the source area and the initial yield strength is almost at the limit to stability, the remolding parameter can become critical because it determines whether the yield strength decreases more rapidly or less rapidly than the slope angle as the slide propagates downslope. In contrast, tsunami genesis is mostly determined by the acceleration of the slide in the *early* phase as well as by the rate of retrogression. These quantities depend directly on $\tau_{y,0}$ in the very beginning and increasingly on $\Gamma$ as the evacuation of the release area progresses. Note, however, that the case-specific critical values of the parameters depend crucially on the size of the slide and the bathymetry.

Including nonzero added mass reduces the landslide acceleration and hence the induced tsunami. Simulations with $C_m = 0.1$ and reduced soil strength parameters ($\tau_{y,0} = 8\,\text{kPa}$, $\tau_{y,\infty} = 3\,\text{kPa}$, $\Gamma = 5 \times 10^{-3}$; not shown) produced almost identical results as the best-fit simulations for $C_m = 0$ discussed above, with offshore water elevations deviating by ±5–10% at individual points. For $C_m = 0.3$ the water elevations near the observation points are on average 30% lower than the best fit simulations, with still larger deviations

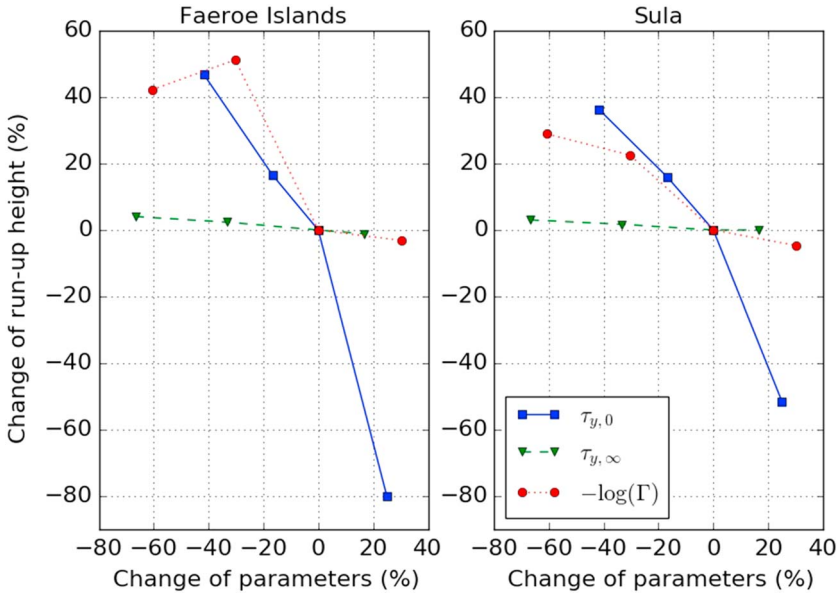


**Figure 14.** Parameter sensitivity tests for the maximum tsunami heights at two locations. The changes of the maximum tsunami height at the Faroe Islands and Sula are shown with respect to the change of parameters. The maximum tsunami heights in both locations are rather sensitive to the choice of $\tau_{y,0}$ and $\Gamma$.

(too small water elevations compared to paleo-tsunami observations) at the Faroes and Shetland Islands. For $C_m = 0.5$ we see the same pattern; here the water elevations near the observation points are on average 64% lower than the best-fit simulations. Hence, increasing the added mass has a strong adverse effect on the generated tsunami elevation, and for the largest values of $C_m$ tested, we obtain clearly lower surface elevations in the model than in the field. When added-mass effects are included, landslide motion is retarded. To keep close agreement with paleo-tsunami observations, we therefore needed to reduce the values of the yield-strength parameters. However, it is stressed that these terms represent different aspects of the landslide physics. In this paper, we rather illustrate some trends for representative parameter ranges. Ideally, an even broader study demonstrating the covariation of different parameters should be carried out in the future.

## 5. Discussion and Conclusion

In this paper, the Storegga Slide and tsunami have been modeled with BingClaw, a combined finite volume and finite difference Eulerian model with visco-plastic Herschel-Bulkley rheology. The landslide is coupled to hydrodynamic long-wave models run in hydrostatic mode to simulate the tsunami generation. In the present analysis, sensitivity studies are carried out to determine the link between soil parameters and the landslide tsunamigenic strength. A crucial point in the sensitivity study is the simultaneous use of landslide runout and paleo-tsunami observations to constrain the uncertainty in the landslide parameter values. Combining these data with our numerical simulations, it is first shown that the landslide runout distance is primarily controlled by the remolded yield strength of the landslide material. In contrast, the initial yield strength together with the soil remodling parameter controls the tsunami genesis. In the present case, the availability of unique paleo-tsunami data allowed us to narrow down the admissible range of landslide parameters significantly. On the other hand, such data are rarely available when analyzing major prehistoric landslides. Matching the landslide runout distance, which is normally the only quantity available for a landslide deposit, we obtain an appreciable uncertainty range in landslide speed and acceleration, which significantly influences the tsunami generation. Hence, past studies using only the landslide runout distance as the constraining parameter should inherit a pronounced uncertainty in runup height. The present analysis therefore provides a first example of ranges for visco-plastic soil parameters for a previous landslide tsunami that may serve as input for possible related hazard studies.

For Storegga, the transition from blocky, intact material to visco-plastic flow probably took place within minutes. Compared to traditional single-block models, BingClaw gives much larger initial acceleration. However, a single-block model tuned to give comparable initial acceleration would generate tsunamis more efficiently than BingClaw, where only a fraction of the total landslide mass is mobilized in the beginning of the slide event. Topographic channeling and lateral spreading also influence wave generation in BingClaw. A retrogressive block model that assumes that one block must be fully mobilized before the next block is released represents an even less efficient generation mechanism that is not sufficient to generate a tsunami of the scale observed for Storegga (see the supporting information).

The dynamic soil parameters in the BingClaw simulations were tuned further to match the observed landslide runout, providing excellent agreement with the major lobe structures of the Storegga slide identified in the morphologic analysis of Haflidason et al. (2004). For the subset of simulations reproducing the landslide runout, we further optimized the landslide parameters to minimize the error between the tsunami simulations and paleo-tsunami observations, obtaining a significantly better agreement compared to previous models.

A 2HD landslide model taking into account topographic effects such as BingClaw has greatly improved our capability to explain the runout of past major submarine landslides, as shown in this paper as well as in Løvholt et al. (2017, 2018). In addition, we show herein for the first time that the numerical model is consistent with asymptotic solutions of the governing model equations as well as experimental data for simplified laboratory studies. Furthermore, coupling a 2HD landslide model with an advanced rheological formulation to a robust and precise tsunami solver has significantly advanced our understanding of the Storegga Slide and, more generally, the link between landslide soil parameters and tsunami generation. For Storegga, good agreement with all observed tsunami runup heights in the near- and far-field can only be achieved if the early phase of the landslide motion is reproduced correctly with regard to the spatial distribution of landslide motion and the temporal evolution of the flow velocity. Thanks to the visco-plastic rheology with a simple remolding model, BingClaw can mimic the overall progression of retrogressive release of the Storegga

Slide. In this way, high acceleration in the startup phase is combined with progressively increasing mass, apparently giving the correct balance between efficiently generating the large Storegga Slide tsunami and avoiding excessive wave generation.

While it has been generally accepted for more than a decade that the Storegga Slide developed retrogressively, the landslide evolution has not been modeled in detail taking into account topography effects. Neither has information on the generated tsunami been used to constrain the landslide dynamics and kinematics, with regard to both the speed of retrogressive lateral spreading and downslope velocity, despite the direct link between the two phenomena. Moreover, previous attempts to model the Storegga Slide runout (De Blasio et al., 2004) and tsunami runup (Bondevik et al., 2005) present inconsistent landslide velocities. In the present model, we move closer to a unified representation of the landslide and tsunami: Our modeled maximum velocities are close to 60 m/s in the constriction at the distal end of the release area, resembling the front velocities obtained with BING (De Blasio et al., 2004), whereas the velocity of frontal landslide progression typically is in the range 30–40 m/s, similar to or slightly larger than the block velocities proposed by Bondevik et al. (2005).

Furthermore, our success in capturing the Storegga Slide tsunami suggests that the lateral retrogressive spread must have propagated fairly rapidly from the location of the initial failure to the upper headwall and that most of the mass was remolded within 30 min. The retrogression speed, derived from the visco-plastic model, would then have been of the order of 30–50 m/s, which is much faster than for the pure retrogressive block model (where simultaneous release of multiple blocks is not possible). The fact that the visco-plastic model gives the best agreement with the tsunami observations implies that the lateral spreading most likely involved quasi-simultaneous release of several landslide blocks, rather than a one-by-one block release as assumed in the retrogressive block model. This inference is also supported by the fact that the retrogressive block model in its present form cannot explain the observed tsunami before the landslide block detaches from the upper headwall because it does not capture such quasi-simultaneous release. Furthermore, the detailed analysis of the last phase of the Storegga Slide by Gauer et al. (2005) shows that many slide blocks are released with short time lags, substantiating our conclusion that the retrogressive slide release proceeded quite rapidly for the Storegga Slide.

**Acknowledgments**
The writing of this paper was funded by the project TsunamiLand (TSUNAMIs induced by large LANDslides, Norwegian Research Council contract 231252/F20), as well as the Norwegian Geotechnical Institute. We thank Tore J. Kvalstad for discussing various aspects of his retrogressive block model with us. We are also grateful for the detailed comments of three anonymous referees. The models applied in this study are found in Kim et al. (2017) and Løvholt et al. (2017).

## References

Berger, M. J., George, D. L., LeVeque, R. J., & Mandli, K. M. (2011). The GeoClaw software for depth-averaged flows with adaptive refinement. *Advances in Water Resources*, *34*, 1195–1206. https://doi.org/10.1016/j.advwatres.2011.02.016

Bondevik, S., Løvholt, F., Harbitz, C. B., Mangerud, J., Dawson, A., & Svendsen, J. I. (2005). The Storegga slide tsunami—Comparing field observations with numerical simulations. *Marine and Petroleum Geology*, *22*(1–2), 195–208.

Bondevik, S., Svendsen, J. I., & Mangerud, J. (1997). Tsunami sedimentary facies deposited by the Storegga tsunami in shallow marine basins and coastal lakes, western Norway. *Sedimentology*, *44*, 1115–1131.

Bryn, P., Berg, K., Forsberg, C. F., Solheim, A., & Kvalstad, T. J. (2005). Explaining the Storegga Slide. *Marine and Petroleum Geology*, *22*(1–2), 11–19. https://doi.org/10.1016/j.marpetgeo.2004.12.003

Castro, M. J., LeFloch, P. G., Mu-Ruiz, M. L., & Pars, C. (2008). Why many theories of shock waves are necessary: Convergence error in formally path-consistent schemes. *Journal of Computational Physics*, *227*(17), 8107–8129. https://doi.org/10.1016/j.jcp.2008.05.012

Chaytor, J., ten Brink, U., Solov, A., & Andrews, B. (2009). Size distribution of submarine landslides along the U.S. Atlantic margin. *Marine Geology*, *264*, 16–27.

Clawpack Development Team (2015). Clawpack software version 5.3.1. https://doi.org/10.5281/zenodo.50982

De Blasio, F., Elverhøi, A., Issler, D., Harbitz, C., Bryn, P., & Lien, R. (2005). On the dynamics of subaqueous clay-rich gravity mass flows – the giant Storegga Slide, Norway. *Marine and Petroleum Geology*, *22*(1–2), 179–186. https://doi.org/10.1016/j.marpetgeo.2004.10.014

De Blasio, F. V., Engvik, L., Harbitz, C. B., & Elverhøi, A. (2004). Hydroplaning and submarine debris flows. *Journal of Geophysical Research*, *109*, C01002. https://doi.org/10.1029/2002JC001714

Elverhøi, A., Issler, D., De Blasio, F. V., Ilstad, T., Harbitz, C. B., & Gauer, P. (2005). Emerging insights into the dynamics of submarine debris flows. *Natural Hazards and Earth System Sciences*, *5*, 633–648.

Enet, F., & Grilli, S. T. (2007). Experimental study of tsunami generation by three-dimensional rigid underwater landslides. *Journal of Waterway, Port, Coastal, and Ocean Engineering*, *133*(6), 442–454. https://doi.org/10.1061/(ASCE)0733-950X(2007)133:6(442)

Fine, I. V., Rabinovich, A. B., Bornhold, B., Thomson, R. E., & Kulikov, E. A. (2005). The Grand Banks landslide-generated tsunami of November 18, 1929: Preliminary analysis and numerical modelling. *Marine Geology*, *215*, 45–57.

Fruergaard, M., Piasecki, S., Johannessen, P. N., Noe-Nygaard, N., Andersen, T. J., Pejrup, M., & Nielsen, L. H. (2015). Tsunami propagation over a wide, shallow continental shelf caused by the Storegga slide, southeastern North Sea, Denmark. *Geology*, *43*(12), 1047–1050. https://doi.org/10.1130/G37151.1

Gauer, P., Kvalstad, T. J., Forsberg, C. F., Bryn, P., & Berg, K. (2005). The last phase of the Storegga Slide: Simulation of retrogressive slide dynamics and comparison with slide-scar morphology. *Marine and Petroleum Geology*, *22*(1–2), 171–178. https://doi.org/10.1016/j.marpetgeo.2004.10.004

George, D. L., & Iverson, R. M. (2014). A depth-averaged debris-flow model that includes the effects of evolving dilatancy. ii. Numerical predictions and experimental tests. *Proceedings of the Royal Society A*, *470*(2170), 20130820. https://doi.org/10.1098/rspa.2013.0820

Grilli, S. T., & Watts, P. (2005). Tsunami generation by submarine mass failure. I: Modeling, experimental validation, and sensitivity analyses. *Journal of Waterway, Port, Coastal, and Ocean Engineering*, *131*(6), 283–297.

Gylfadóttir, S. S., Kim, J., Helgason, J. K., Brynjólfsson, S., Höskuldsson, Á., Jóhannesson, T., et al. (2017). The 2014 Lake Askja rockslide-induced tsunami: Optimization of numerical tsunami model using observed data. *Journal of Geophysical Research: Oceans*, *122*, 4110–4122. https://doi.org/10.1002/2016JC012496

Haflidason, H., Lien, R., Sejrup, H. P., Forsberg, C. F., & Bryn, P. (2005). The dating and morphometry of the Storegga Slide. *Marine and Petroleum Geology*, *22*, 123–136.

Haflidason, H., Sejrup, H. P., Nygård, A., Mienert, J., Bryn, P., Lien, R., et al. (2004). The Storegga slide: architecture, geometry and slide development. *Marine Geology*, *213*(1–4), 201–234. https://doi.org/10.1016/j.margeo.2004.10.007

Harbitz, C. B. (1992). Model simulations of tsunamis generated by the Storegga Slides. *Marine Geology*, *105*, 1–21. https://doi.org/10.1016/0025-3227(92)90178-K

Harbitz, C., Løvholt, F., & Bungum, H. (2014). Submarine landslide tsunamis: How extreme and how likely? *Natural Hazards*, *72*(3), 1341–1374. https://doi.org/10.1007/s11069-013-0681-3

Hill, J. C., Brothers, D. S., Craig, B. K., ten Brink, U. S., Chaytor, J. D., & Flores, C. H. (2017). Geologic controls on submarine slope failure along the central U.S. Atlantic margin: Insights from the Currituck Slide Complex. *Marine Geology*, *385*, 114–130. https://doi.org/10.1016/j.margeo.2016.10.007

Hill, J., Collins, G. S., Avdis, A., Cramer, S. C., & Piggot, M. (2014). How does multiscale modelling and inclusion of realistic palaeobathymetry affect numerical simulation of the Storegga Slide tsunami? *Ocean Modelling*, *83*, 11–25. https://doi.org/10.1016/j.ocemod.2014.08.007

Huang, X., & García, M. H. (1997). A perturbation solution for Bingham-plastic mudflows. *Journal of Hydraulic Engineering (ASCE)*, *123*(11), 986–994. https://doi.org/10.1061/(ASCE)0733-9429(1997)123:11(986)

Huang, X., & García, M. H. (1998). A Herschel–Bulkley model for mud flow down a slope. *Journal of Fluid Mechanics*, *374*, 305–333.

Imran, J., Parker, G., Locat, J., & Lee, H. (2001). 1-D numerical model of muddy subaqueous and subaerial debris flows. *Journal of Hydraulic Engineering (ASCE)*, *127*(11), 959–968. https://doi.org/10.1061/(ASCE)0733-9429(2001)127:11(959)

Issler, D. (2010). *The shear-layer thickness in the initial flow phase of a Herschel–Bulkley fluid*. Oslo Norway: NGI Technical Note 20180080-03-TN Norwegte.

Kajiura, K. (1963). The leading wave of a tsunami. *Bulletin of the Earthquake Research Institute*, *41*, 535–571.

Kelfoun, K., Giachetti, T., & Labazuy, P. (2010). Landslide-generated tsunamis at Réunion Island. *Journal of Geophysical Research*, *115*, F04012. https://doi.org/10.1029/2009JF001381

Kim, J., Pedersen, G. K., Løvholt, F., & LeVeque, R. J. (2017). A Boussinesq type extension of the Geoclaw model—A study of wave breaking phenomena applying dispersive long wave models. *Coastal engineering*, *122*, 75–86. https://doi.org/10.1016/j.coastaleng.2017.01.005

Kvalstad, T., Andresen, L., Forsberg, C. F., Berg, K., Bryn, P., & Wangen, M. (2005). The Storegga Slide: Evaluation of triggering sources and slide mechanics. *Marine and Petroleum Geology*, *22*(1–2), 245–256. https://doi.org/10.1016/j.marpetgeo2004.10.019

Laberg, J. S., & Vorren, T. O. (2000). The Trænadjupet slide, offshore Norway—Morphology, evacuation and triggering mechanisms. *Marine Geology*, *171*, 95–114.

LeVeque, R. J. (2002). Finite volume methods for hyperbolic problems, *Cambridge texts in applied mathematics* (Vol. 31, pp. 580). Cambridge, UK: Cambridge University Press. https://doi.org/10.1017/CBO9780511791253

Lee, H. J. (2009). Timing of occurrence of large submarine landslides on the Atlantic Ocean margin. *Marine Geology*, *264*, 53–64.

Løvholt, F., Bondevik, S., Laberg, J. S., Kim, J., & Boylan, N. (2017). *Some giant submarine landslides do not produce large tsunamis* (Vol. 44, pp. 8463–8472). https://doi.org/10.1002/2017gl074062

Løvholt, F., Harbitz, C. B., & Haugen, K. B. (2005). A parametric study of tsunamis generated by submarine slides in the Ormen Lange/Storegga area off western Norway. *Marine and Petroleum Geology*, *22*(1–2), 219–231.

Løvholt, F., Pedersen, G., & Harbitz, C. B. (2016). Tsunami-genesis due to retrogressive landslides on an inclined seabed. In G. Lamarche, et al. (Eds.), *Submarine mass movements and their consequences: 7th symposium* (Vol. 41, pp. 569–578). Cham: Springer. https://doi.org/10.1007/978-3-319-20979-1_57

Løvholt, F., Pedersen, G., Harbitz, C. B., Glimsdal, S., & Kim, J. (2015). On the characteristics of landslide tsunamis. *Phil. Trans. R. Soc. London A*, *373*(2053), 20140376. https://doi.org/10.1098/rsta.2014.0376

Løvholt, F., Schulten, I., Mosher, D., Harbitz, C., & Krastel, S. (2018). Modelling the 1929 Grand Banks slump and landslide tsunami. Subaqueous Mass Movements, Special Publications, vol. 477, The Geological Society of London, https://doi.org/10.1144/SP477.28

Lynett, P. J., Borrero, J. C., Liu, P. L.-F., & Synolakis, C. E. (2003). Field survey and numerical simulations: A review of the 1998 Papua New Guinea Tsunami. *Pure and Applied Geophysics*, *160*, 2119–2146.

Mandli, K. T., Ahmadia, A. J., Berger, M., Calhoun, D., George, D. L., Hadjimichael, Y., et al. (2016). Clawpack: building an open source ecosystem for solving hyperbolic PDEs. *PeerJ - Computer Science*, *e68*, 2. https://doi.org/10.7717/peerj-cs.68

Masson, D. G., Harbitz, C. B., Wynn, R. B., Pedersen, G., & Løvholt, F. (2006). Submarine landslides—Processes, triggers and hazard prediction. *Philosophical Transactions of the Royal Society A*, *364*, 2009–2039.

Mohrig, D., Elverhøi, A., & Parker, G. (1999). Experiments on the relative mobility of muddy subaqueous and subaerial debris flows, and their capacity to remobilize antecedent deposits. *Marine Geology*, *154*, 117–129.

Mohrig, D., Whipple, K. X., Hondzo, M., Ellis, C., & Parker, G. (1998). Hydroplaning of subaqueous debris flows. *Geological Society of America Bulletin*, *110*(3), 387–394.

Okal, E. A., & Synolakis, C. E. (2004). Source discriminants for near-field tsunamis. *Geophysical Journal International*, *158*(3), 899–912.

Pastor, M., Blanc, T., Haddad, B., Petrone, S., Sanchez Morles, M., Drempetic, V., et al. (2014). Application of a SPH depth-integrated model to landslide run-out analysis. *Landslides*, *11*, 793–812. https://doi.org/10.1007/s10346-014-0484-y

Pastor, M., Haddad, B., Sorbino, G., Cuomo, S., & Drempetic, V. (2009). A depth-integrated, coupled SPH model for flow-like landslides and related phenomena. *International Journal for Numerical and Analytical Methods Geomechanics*, *33*(2), 143–172. https://doi.org/10.1002/nag.705

Romano, A., Di Risio, M., Bellotti, G., Molfetta, M. G., Damiani, L., & De Girolamo, P. (2016). Tsunamis generated by landslides at the coast of conical islands: experimental benchmark dataset for mathematical model validation. *Landslides*, *13*(6), 1379–1393. https://doi.org/10.1007/s10346-016-0696-4

Romundset, A., & Bondevik, S. (2011). Propagation of the Storegga tsunami into ice-free lakes along the southern shores of the Barents Sea. *Journal of Quaternary Science*, *26*(5), 457–462. https://doi.org/10.1002/jqs.1511

Salmanidou, D. M., Guillas, S., Georgiopoulou, A., & Dias, F. (2017). Statistical emulation of landslide-induced tsunamis at the Rockall Bank, NE Atlantic. *Proceedings of the Royal Society of London A*, *473*(2200). https://doi.org/10.1098/rspa.2017.0026

Smith, D. E., Shi, S., Cullingford, R. A., Dawson, A. G., Dawson, S., Firth, C. R., et al. (2004). The Holocene Storegga Slide tsunami in the United Kingdom. *Quaternary Science Reviews*, *23*(23–24), 2291–2321. https://doi.org/10.1016/j.quascirev.2004.04.001

Synolakis, C. E., Bardet, J.-P., Borrero, J. C., Davies, H. L., Okal, E. A., Silver, E. A., et al. (2002). The slump origin of the 1998 Papua New Guinea Tsunami. *Proceedings of the Royal Society of London A*, *458*(2020), 763–789. https://doi.org/10.1098/rspa.2001.0915

Talling, P. J. (2014). On the triggers, resulting flow types and frequencies of subaqueous sediment density flows in different settings. 50th Anniversary Special Issue. *Marine Geology*, *352*(0), 155–182. https://doi.org/10.1016/j.margeo.2014.02.006

Tappin, D. (2010). Mass transport events and their tsunami hazard: Submarine mass movements and their consequences. In D. C. Mosher et al. (Eds.), *Submrine Mass Movements and Their Consequences*, Advances in Natural and Technological Hazards Research (pp. 667–684). Dordrecht, Netherlands: Springer Science.

Tappin, D. R., Watts, P., & Grilli, S. T. (2008). The Papua New Guinea tsunami of 17 July 1998: Anatomy of a catastrophic event. *Natural Hazards and Earth System Sciences*, *8*, 243–266.

Wagner, B., Bennike, O., Klug, M., & Cremer, H. (2007). First indication of Storegga tsunami deposits from East Greenland. *Journal of Quaternary Science*, *22*(4), 321–325. https://doi.org/10.1002/jqs.1064

Watts, P. (2000). Tsunami features of solid block underwater landslides. *Journal of Waterway, Port, Coastal, and Ocean Engineering*, *126*(3), 144–152.

Yavari-Ramshe, S., & Ataie-Ashtiani, B. (2016). Numerical modeling of subaerial and submarine landslide-generated tsunami waves—Recent advances and future challenges. *Landslides*, *13*(6), 1325–1368.